DOI: 10.1002/((please add manuscript number))
Article type: Communication

Bulky End-Capped [1]Benzothieno[3,2-*b*]benzothiophenes: Reaching High Mobility Organic Semiconductors by Fine Tuning of the Crystalline Solid-State Order

Guillaume Schweicher, Vincent Lemaur, Claude Niebel, Christian Ruzié, Ying Diao, Osamu Goto, Wen-Ya Lee, Yeongin Kim, Jean-Baptiste Arlin, Jolanta Karpinska, Alan R. Kennedy, Sean R. Parkin, Yoann Olivier, Stefan C. B. Mannsfeld, Jérôme Cornil, Yves H. Geerts, Zhenan Bao**

Dr. G. Schweicher, Dr. Y. Diao, Dr. O. Goto, Dr. W.-L. Lee, Y. Kim, Prof. Z. Bao
Department of Chemical Engineering
Stanford University
381 North-South Mall, Stanford, CA 94305, USA
E-mail: zbao@stanford.edu

Dr. V. Lemaur, Dr. Y. Olivier, Dr. J. Cornil
Laboratory for Chemistry of Novel Materials
University of Mons-UMONS
Place du Parc 20, B-7000 Mons, Belgium

Dr. C. Niebel, Dr. C. Ruzié, Dr. J.-B. Arlin, Dr. J. Karpinska, Prof. Y. H. Geerts
Laboratoire de Chimie des Polymères
Faculté des Sciences
Université Libre de Bruxelles (ULB)
CP206/1, Boulevard du Triomphe, 1050 Brussels, Belgium
E-mail: ygeerts@ulb.ac.be

Dr. A. R. Kennedy
Department of Pure and Applied Chemistry
University of Strathclyde
295 Cathedral Street, Glasgow G1 1XL, Scotland

Dr. S. R. Parkin
Department of Chemistry
University of Kentucky
Lexington, KY 40506-0055, USA

Prof. S. C. B. Mannsfeld
Center for Advancing Electronics Dresden
Technische Universität Dresden
01062 Dresden, Germany

Keywords: organic semiconductor, single crystal, high mobility, organic transistor

For the past two decades, organic electronics has emerged as a field of intense research gaining considerable industrial interest due to its potential revolutionary applications such as flexible displays and sensors.[1] In spite of tremendous progress in molecular design, engineering and processing, only few small molecule organic semiconductors (OSC) have reached field-effect mobilities higher than 10 $cm^2 V^{-1} s^{-1}$, typically with single crystal devices.[2] Moreover, as a result of the anisotropic nature of charge transport in these weakly van der Waals bounded systems, preferential alignment along the highest charge transport axis is necessary to harvest the full potential of single crystals.[3, 4] However, uniform and large area production of single crystals with controlled size, shape and orientation at designated locations on a substrate remains challenging and hampers their use for practical applications.[4, 5]

The large body of work on organic semiconductors developed over the years provides us with clues for the rational design of new promising small molecule materials. The excellent performance of rubrene and 6,13-bis(triisopropylsilylethynyl)pentacene (TIPS-pentacene) come from their respective 2D layered herringbone and brickwall packing, results of the steric hindrance of the bulky substituents.[6] However, their packing structures also give rise to pronounced in-plane charge transport anisotropy.[7]

Among the reported molecular semiconductors, [1]benzothieno[3,2-*b*]benzothiophene (BTBT)[8] and dinaphtho[2,3-*b*:2',3'-*f*]thieno[3,2-*b*]thiophene (DNTT)[9] have shown some of the highest mobilities reported to date.[4, 10] Combined with a high chemical stability and an easy synthetic route, these molecules are attractive core units for structure property relationship studies. Moreover, multiple successful derivatization attempts of these aromatic cores have already been reported in the literature.[11] It is also worth mentioning that the brand new promising V and N-shaped materials developed by Okamoto, Takeya and coworkers.[12]

In a previous study, the Bao group demonstrated the ability to modify charge transport properties of oligothiophenes *via* fine tuning of their crystal packing structures by the addition of bulky pendant groups.[13] This gave rise to a rational designed organic semiconductor, trimethyl-[2,2';5',2'';5'',2''']quaterthiophen-5-yl-silane (4TTMS), which has an in-plane isotropic mobility of 0.1 $cm^2 V^{-1} s^{-1}$ recorded with physical vapor transport (PVT) grown single crystals field-effect transistors (FETs).[14]

In this paper, we report the substitution of the BTBT core with end groups of different bulkiness in an attempt to modulate the charge transport properties of the resulting materials through changing the molecular packing lattice in in the x, y herringbone plane in order to potentially achieve high charge carrier mobility above 10 $cm^2 V^{-1} s^{-1}$. This work allowed us to identify 2,7-di-*tert*-butylBTBT (**ditBu-BTBT**) as a new high-performance organic semiconductor with large and well-balanced transfer integrals as evidenced by quantum-chemical calculations. Single-crystal FETs showed remarkable saturation mobility as high as 17 $cm^2 V^{-1} s^{-1}$ while solution processed thin film showed mobility as high as 3.7 $cm^2 V^{-1} s^{-1}$.

The chemical structures of investigated molecules are classified by ascending order of bulkiness: mono-isopropyl **iPr**, di-isopropyl **diiPr**, mono-tertbutyl **tBu**, di-tertbutyl **ditBu**, bis(trimethylsilyl) **diTMS** (**Figure 1a**). The full synthetic procedures are detailed in the Supporting Information. The thermal behavior of the different BTBTs was investigated by thermogravimetric analysis (TGA) and differential scanning calorimetry (DSC). Sublimation and/or evaporation of the materials occurs at temperatures ranging from 260 to 290 °C (Figure S1a), giving access to easy vacuum sublimation purification and vapor growth of single crystals. DSC traces as well as transition temperatures and their associated energies are presented in Figure S1b and Table S1. **ditBu-BTBT** and **diTMS-BTBT** show the highest

melting points (277.1 and 215.3 °C, respectively) with a crystal-crystal transition at lower temperatures (71.2 and 154.7 °C, respectively). Interestingly, the TMS substitution of the aromatic core gives rise to an almost 80 °C increase in the reversible crystal-crystal transition (Figure S1c, d). On the other hand, it also reduces the close molecular packing, as observed by the 60 °C decrease of the melting point.

Single crystals of the different BTBT derivatives were grown by PVT (growth parameters are presented in Table S2) in order to investigate their molecular packing and charge transport properties. Structure determination was realized by single crystal X-ray diffraction and the complete crystal data are available in Table S3. The bulky end-capped BTBTs adopt a standard layer-by-layer herringbone packing motif with a tilt angle of the molecules within a herringbone layer, δ, being determined by the terminal substitution (Figure 1b, the tilt angle of the molecule is defined as the angle between the plane of the aromatic core and the normal direction to the herringbone layer plane). Indeed, the bulkiness of the TMS substitution imposes a severe tilt on the molecules (51.3°) while the tilt is reduced for iPr substitution [**diiPr-BTBT** (42.5°) - **iPr-BTBT** (35.8°)] and more reduced for the tBu-derivatives [**ditBu-BTBT** (40.5°) - **tBu-BTBT** (0°)]. We attribute the tilt angle achieved for the iPr compounds to its asymmetry and reduced bulkiness, inducing more disorder and allowing interactions with the neighboring layers (**iPr-BTBT**). Monosubstituted aromatic cores present an alternating upside down arrangement of the molecules allowing the cores to arrange more vertically (smaller tilt angle compared to disubstituted derivatives). Moreover, both of these asymmetric molecular compounds also possess a higher crystalline symmetry (orthorhombic vs monoclinic packing achieved for the other compounds). Finally, it is worth mentioning that both **tBu-BTBT** and **diiPr-BTBT** crystals possess certain amounts of disorder (see Figure S2) in their molecular packing that could have a direct impact on their charge transport

properties, as will be explained later. CIFs for the different BTBT derivatives are summarized in the supporting materials of this paper.

In order to have a clear quantitative and visual insight into the intermolecular interactions, Hirshfeld surfaces of the bulky end-capped BTBTs and their relative 2D fingerprints were calculated using Crystal Explorer (Figure S3). Interestingly, the ditBu substitution of the BTBT core induces a deformation of the molecular packing, leading to the absence of any dominant interactions, which can be seen in the Hirshfeld surfaces by the bright red areas. All the other BTBT derivatives as well as **C12-BTBT**, used for comparison, present a molecular packing impacted by the dominant S···S and/or C···S interactions (H···S in the case of **diTMS-BTBT**). A look at the percentage contributions of the various close intermolecular contacts for the different BTBT derivatives (Figure S4) highlights the effect of the bulkiness of the ditBu and diTMS substitutions, hampering the contribution of the S···S and C···S interactions on the resulting molecular packing. The sum of their contributions reaches 7% in the case of **ditBu-BTBT**, while the bulkier **diTMS-BTBT** only provides a contribution of 3.8% (other bulky end-capped BTBTs show values ranging from 9.9 to 15.7% while **BTBT-C12** contribution is 6.7%). As recently reported by Kreyes et al., the bulkiest investigated substitution, diTMS, is expected to have a more detrimental effect on the charge transport properties of the material.[15] Indeed, such a substitution clearly increases the distance between neighboring molecules within the 2D in-plane herringbone packing.

All the compounds formed thin, nearly two-dimensional platelet crystals, ideal for single crystal transistor device fabrication except **iPr-BTBT,** which favored the growth of needles. The observed crystal habits clearly fit their crystal growth morphologies calculated by the Hartman theory, and are visible in Figure 1d (a detailed indexation of the attachment energies and corresponding percentage of total facet area of the most dominant faces in the growth morphology is presented in Table S4).[16] **iPr-BTBT**, with its stronger out-of-plane interaction

opens the way for acircular growth, as observed by the formation of thick needle-like single crystals. Lower performances are expected from devices built from this material as a result of the higher access resistance.[2] Moreover it is worth noting that the flatter disk-like morphology observed for **ditBu-BTBT** is likely the result of its almost uniform in-plane interactions.

Figure 2 presents the most important energetic parameters relative to the charge transport properties of our BTBT derivatives in a hopping regime transport: the reorganization energy, the transfer integral and the ionization potential; note that the hopping regime is a good starting point to model charge transport in devices operating at room temperature due to the localization of the charge carriers induced by lattice thermal fluctuations.[17] The reorganization energies (λ) and transfer integrals (J) between the highest occupied molecular orbitals (HOMOs, Figure 2) of the individual units were calculated at the Density Functional Theory (DFT) level, see Experimental Section. The reorganization energies are very close for the different bulky end-capped BTBTs and range between 0.24 and 0.29 eV, the highest value being obtained for **diTMS-BTBT**. The calculated transfer integral values point to a strong electronic overlap of the HOMO levels, with marked differences among the interacting dimers depending on substituents. These variations are critical and have to be as small as possible in order to approach isotropic charge transport properties. **ditBu-BTBT** presents large and well-balanced transfer integrals in the plane (60 meV, 53 meV, 12% deviation) compared to the other derivatives. Moreover, these values are larger and more balanced compared to those achieved for the well-known high-performance **C12-BTBT** (56 meV, 43 meV, 23% deviation). The anisotropy of the field-effect mobility in a pure hopping regime has been calculated with a Kinetic Monte Carlo approach (see Experimental Section) as a function of the crystal packing for the different OSCs and is presented in Figure S5. As expected, these plots highlight the relative anisotropy of charge transport in the different derivatives and in particular the very interesting almost perfect isotropic transport achieved in **ditBu-BTBT**

(Figure 3g). Finally, the ionization potentials (IPs) were measured by photoelectron spectroscopy on thin films spin coated (10 mg ml^{-1} in chlorobenzene – thickness ranging from 60 to 90 nm) on glass substrates. The IPs of the different BTBT derivatives, ranging from 5.5 to 5.8 eV, are presented in Figure 2b. The large variation in IP levels as a function of molecular packing highlights the strong effect of molecular packing on electronic structures. The extremely deep values of the experimental IPs required us to use a top contact OFET configuration with the application of a MoO_3 hole-injection layer (electron affinity goes from -6.7 eV for a freshly evaporated layer till -5.2 eV after exposure to moisture present in air).[18]

Single crystal charge transport properties of the bulky end-capped BTBTs were evaluated by using thin platelet PVT-grown crystals. Transistors were fabricated by evaporation of a MoO_3 layer and Au electrodes through a shadow mask on top of the single crystals laminated on octadecyltrimethoxysilane (OTS) treated 300 nm thermally grown SiO_2 substrates. The resulting bottom-gate top-contact device architecture is presented in Figure 3a. In order to avoid any loss of performance due to the exposure of MoO_3 to the atmosphere, devices were directly transferred to a N_2-filled glovebox (after electrodes evaporation) before subsequent measurements.

The FET performances are presented in Figure 2b. At first sight, it is clear that performances are directly impacted by the deep ionization potentials of our materials whose devices present large V_{th} values combined to low mobilities (OFETs characteristics of the different BTBT derivatives are presented in Figure S6).[19] Moreover, the structural disorder present in **tBu-BTBT** and **diiPr-BTBT** demonstrates its propensity to impede charge transport, as evidenced by the poor performance of **tBu-BTBT** devices and our inability to record any FET response for **diiPr-BTBT**. However, **ditBu-BTBT** clearly demonstrates its potential with saturation mobility up to 17 $cm^2 V^{-1} s^{-1}$ (average 7.1 $cm^2 V^{-1} s^{-1}$) accompanied by a very high on/off ratio

of 10^9 (Figure 3b-d shows the optical micrograph and OFET characteristics of a **ditBu-BTBT** device presenting a field-effect mobility of 17 $cm^2 V^{-1} s^{-1}$).

GIXD performed on thin platelet single crystals of **ditBu-BTBT** (laminated on a silicon substrate) confirmed their molecular packing in the monoclinic phase (Figure S7 and Table S6, also including powder diffractograms and refined parameters achieved through specular X-ray diffraction of a powder sample). As a result of the top contact geometry, together with the deep ionization potentials and higher hole-injection barriers, our mobility distribution is directly related to the thickness distribution of the selected single crystals used to fabricate the devices (the importance of the strong acceptor in the contacts is presented in the supporting information with results obtained using only Au and another strong acceptor, V_2O_5, presented in Table S7 and Figure S8). The mobility histogram of our 42 devices realized with **ditBu-BTBT** single crystals and its thickness dependence (evaluated by profilometry) is presented in Figure 3e-f. Thinner crystals indeed exhibit higher field-effect mobilities due to the lower contact resistance.[20]

The gate voltage sweep rate dependence of the nominal mobility of our devices has also been investigated in order to avoid any over-estimation of the extracted value. Chen et al. have recently reported the influence of the gate-voltage sweep rate in the case of trap dominated FETs exhibiting a dispersive transport.[21] Our devices do not show any significant variation of the extracted mobility for gate voltage sweeping rates ranging from 0.5 V s^{-1} to 19 V s^{-1} (see Figure S9), confirming the good charge transport performances of **ditBu-BTBT**.

Given the high performances of **ditBu-BTBT** and its good solubility in various solvents, solution-sheared films were fabricated to demonstrate its potential for solution-processed devices. Non optimized shearing conditions (solution of 2 mg ml^{-1} in tetralin sheared at 0.4

mm s^{-1}) allowed us to produce devices presenting an average mobility of 2.4 $cm^2 V^{-1} s^{-1}$ (max 3.7 $cm^2 V^{-1} s^{-1}$) with ribbon-like crystalline domains in thin films. Optical micrograph, AFM image and FET characteristics of a solution-sheared film are presented in Figure S10.

In summary, we have designed and synthesized a series of bulky end-capped BTBTs with the aim of tuning their crystalline packing. A combined theoretical and experimental study allowed us to identify 2,7-di-*tert*-butylBTBT as a new high-performance solution processable organic semiconductor with large and well-balanced transfer integrals as evidenced by quantum-chemical calculations. The fine tBu substitution improves the orbital overlap of the molecules within their crystalline architecture. PVT grown single crystal field-effect transistors show very high hole mobilities, reaching 17 $cm^2 V^{-1} s^{-1}$. Further modifications of the molecular structure of **ditBu-BTBT** aiming to reduce its ionization potential and improve its molecular packing are currently under investigation.

Experimental Section

Materials: Octadecyltrimethoxysilane (OTS) was purchased from Gelest and used as received (storage under an argon atmosphere to prevent hydrolysis). Molybdenum (VI) oxide (MoO_3) and vanadium (V) oxide (V_2O_5) were purchased from Aldrich. Highly doped *n*-type Si (100) wafers (resistivity < 0.005 Ω cm, Silicon Quest) were used as the substrates for TFT fabrication. A 300 nm SiO_2 layer (capacitance C_i = 11.5 nF cm^{-2}) was thermally grown onto the Si substrates as a gate dielectric.

Synthesis: The full synthetic procedures of the different bulky end-capped [1]benzothieno[3,2-*b*]benzothiophenes are detailed in the Supporting Information.

Crystal growth: Single crystals were grown by the physical vapor transport method[22] at atmospheric pressure in a high-purity argon flow of 80 sccm; the details of this setup are described elsewhere.[23] Typical growth conditions (temperatures of the sublimation and

growth zone as well as growth durations) are presented in Table S2. Crystals varied in thickness from hundreds of nanometers to several micrometers. Thinnest crystals were mainly selected due to their better performances.[23]

Crystal Analysis: For **ditBu-BTBT** and **diTMS-BTBT** (single crystals grown from solution), data collection and processing was carried out on a Oxford diffraction Xcalibur E diffractometer using Mo Kα radiation[24]; for **tBu-BTBT**, **iPr-BTBT** and **diiPr-BTBT** (single crystals grown by sublimation), data were recorded on a Bruker-Nonius X8 Proteum CCD diffractometer using Cu Kα radiation[25]. The crystal structures were solved using SHELXS and refined by full matrix least-squares methods based on F^2 using SHELXL97 or SHELXL-2014.[26] The displacement parameters of all non-H atoms were treated anisotropically. H atoms were placed at calculated positions using suitable riding models with fixed isotropic thermal parameters [$U_{iso}(H) = 1.2U_{eqv}(C)$ for CH groups and $U_{iso}(H) = 1.5U_{eqv}(C)$ for CH_3]. The relatively high R-values for the vapour-grown crystals, and especially of **tBu-BTBT**, are largely a consequence of poor counting statistics caused by the extreme thinness of the crystals.

CCDC 1008118 (**tBu-BTBT**), 1008119 (**iPr-BTBT**), 1008120 (**diiPr-BTBT**), 1008575 (**ditBu-BTBT**) and 1008576 (**diTMS-BTBT**) contain the supplementary crystallographic data for this paper. These data can be obtained free of charge from The Cambridge Crystallographic Data Centre via www.ccdc.cam.ac.uk/data_request/cif.

Hirshfeld Surface Analysis: Hirshfeld surfaces[27] and the associated fingerprint plots[28] were calculated using Crystal Explorer (Version 3.1)[29], which accepts a structure input file in the CIF format. Bond lengths to hydrogen atoms were set to typical neutron values (C-H = 1.083 Å). For each point on the Hirshfeld isosurface, two distances d_e, the distance from the point to the nearest nucleus external to the surface, and d_i, the distance to the nearest nucleus internal to the surface, are defined. The normalized contact distance (d_{norm}) based on d_e and d_i is given by

$$d_{norm} = \frac{(d_i - r_i^{vdW})}{r_i^{vdW}} + \frac{(d_e - r_e^{vdW})}{r_e^{vdW}}$$

Where r_i^{vdW} and r_e^{vdW} are the van der Waals radii of the atoms. The value d_{norm} is negative or positive depending if the intermolecular contacts are shorter or longer than the van der Waals separations. The parameter d_{norm} displays a surface with a red-white-blue color scheme, where bright red spots highlight shorter contacts, white areas represent contacts around the van der Waals separation, and blue regions are devoid of close contacts.

Crystal Growth Morphology Calculation: Crystal growth morphologies were calculated from the solved crystal structures using the Morphology module of the Materials Studio Package[30] (Compass force field)[31]. The attachment energy (E_{att}) method developed by Hartman was used to determine the relative importance of the different crystallographic faces in the crystal morphology: faces with higher E_{att} (in absolute value) grow faster and have less importance in the final shape and vice versa.[16] This methodology is quite efficient to describe the shape of crystals grown from vapor or from the melt, i.e. without external interactions (solvent molecule by example).

Single-Crystal Device Fabrication: Due to the deep ionization potential of our BTBT-derivatives, single-crystal devices were fabricated in a bottom-gate-top-contact geometry using a doping agent to improve the contacts. Freshly grown single crystals were firstly laminated on octadecyltrimethoxysilane (OTS) treated 300 nm thermally grown SiO_2 substrates. The monolayer was deposited according to a method we published previously.[32] Approximately 7 and 40 nm of molybdenum oxide and gold were thermally evaporated onto the single crystals at a rate of 0.2 Å s^{-1} and 0.5 Å s^{-1} respectively, while rotating the substrate holder, to complete the devices. The electrode dimensions were defined by a shadow mask with a 50 µm channel length (L), and a W/L ratio of 20. The W/L used in the mobility calculation for single-crystal devices was evaluated from the individual crystal used (average of the length of each side of the crystal in contact with the electrodes).

Solution-Sheared Device Fabrication: The shearing substrates were prepared using Si wafer with 300 nm SiO_2 layer functionalized with pentafluoro-phenylpropyltrichlorosilane following the procedure described in previous work.[33] Solution shearing was performed as the following. First, 2 mg ml^{-1} **ditBu-BTBT** solution in tetralin was prepared and then sandwiched between the shearing blade and the substrate. The substrate was heated to 133 °C, and the blade was tilted by 8°. The blade front was separated from the substrate surface by 40 μm. The shearing speed was 0.4 mm s^{-1}. The resulting film thickness was 55 nm on average, measured by AFM. Mobility was channel width corrected.[34]

Device Characterization: Transistors were characterized using a Keithley 4200-SCS semiconductor parameter analyser and standard probe station setup at room temperature in an N_2-filled glovebox. Device parameters were extracted using the standard calculation techniques. The devices were stored in the dark in an N_2-filled glovebox.

Other Characterization Techniques: Optical micrographs were recorded with a cross-polarized optical microscope (Leica DM4000M). Thickness measurements were realized with a Dektak 150 profilometer (Veeco Metrology Group). Tapping mode atomic force microscopy was performed using a Multimode Nanoscope III (Digital Instruments/Veeco Metrology Group). Differential scanning calorimetry and thermogravimetric analysis were realized respectively on a Perkin-Elmer Diamond 6 DSC and a Perkin Elmer Pyris 6 TGA. UV visible and photoelectron spectroscopy in air measurements were recorded on a UV-Vis-NIR spectrophotometer (Cary 6000i) and a Riken Keiki AC-2 photoelectron spectrometer. Specular X-ray diffraction (sXRD) of powders was performed on a Bruker D8 Advance diffractometer, using Cu Kα radiation (λ=1.5418 Å), equipped with a MRI (Material Research Instruments) heating stage for temperature-dependent measurements. Diffraction patterns were collected in the scattered angular range between 1.6° and 60° with an angular resolution of 0.02° per step and a typical counting time of 20 s per step, using θ/θ reflection geometry (the source and detector both move from the horizontal sample plane at the same

angle θ, that is, in specular reflection conditions). GIXD was performed at beam line 11-3 and 1-5 of Stanford Synchrotron Radiation Lightsource (SSRL) at SLAC National Accelerator Laboratory, Menlo Park, CA, United States. The beam energy is 12.73 keV and the incidence angle of X-ray was 0.12°. X-ray diffraction images were collected on 2D image plate (MAR345, 2300×2300 pixels, effective pixel size=150 μ m). The image plate was placed 400 mm from the sample stage. For single crystal samples, rotation stage was employed at beamline 1-5 and the diffraction data was collected at ambient conditions. For thin film samples, helium chamber and heated sample stage were used for detecting polymorphic transitions during sample annealing. The data analysis was performed using the WxDiff software and customized unit cell indexing algorithm.[35]

Quantum-chemical calculations and Kinetic Monte Carlo Simulations: The hole transport properties of all BTBT derivatives have been described using the Marcus-Levich-Jortner formalism. This model assumes that charges are hopping between neighboring molecules and expresses the rate of hole transfer k_{hop} as:[36]

$$\square_{\hbar\square\square} = \frac{4\square^2}{h}\square^2\frac{1}{\sqrt{4\square\square_{\square}\square_{\square}\square}}\sum_{\square}\square\square\square(-\square)\frac{\square^{\square}}{\square!}\square\square\square\left[-\frac{(\square_{\square}+\square\hbar\square+\Delta\square^0)^2}{4\square_{\square}\square_{\square}\square}\right]$$

where S is the Huang-Rhys factor which is related to the internal reorganization energy λ_i ($S = \lambda_i / \hbar\omega$), J the transfer integral, λ_s the external reorganization energy, k_B the Boltzmann constant, T the temperature, $\Delta G°$ the free energy of the reaction and $\hbar\omega$ an effective vibrational mode (carbon-carbon stretching mode) that assists charge transport. The internal reorganization energy entering the Huang-Rhys factor is a parameter that reflects the geometric changes of the molecules involved in the charge transport process upon charge transfer. It has been evaluated at the DFT level (B3LYP/6-31g**) according to the procedure described elsewhere.[37] The $\hbar\omega$ effective stretching mode has been set to 0.2 eV and the

external reorganization energy to the typical value of 0.1 eV.[38] The HOMO transfer integral (J) describes the amplitude of the interactions between the HOMO electronic levels of the two molecules involved in the hole transfer process. This term has been estimated in a fragment approach at the DFT level (B3LYP/DZ) with the ADF package[39] as described elsewhere.[40] Due to the weak energetic disorder in crystals, $\Delta G°$ can be expressed solely as $\Delta G° = e\,\vec{F}\,\vec{d}$, where $\vec{F}$ and $\vec{d}$ are the electric field and distance vectors between mass centers, respectively. Finally, the charge carrier mobility (μ) has been evaluated using a Kinetic Monte Carlo technique with the First Reaction Method algorithm. This technique allows us for the propagation of a single charge carrier in the crystals following a stochastic dynamics where the direction taken by the charge in the crystal in each Monte Carlo cycle is chosen according to the smallest hopping time. The hopping time t_{ij} (rate k_{ij}) between two molecules i and j is determined using the following expression:

$$\square_{\square\square} = -\frac{\square\square(\square)}{\square_{\square\square}}$$

where r is a random number chosen between 0 and 1. The charge carrier mobility is obtained at the end of the simulation as:

$$\square = \frac{\square_{\square\square\square}}{\square_{\square\square\square}\square}$$

where d_{tot} and t_{tot} are the total distance travelled during the Kinetic Monte Carlo simulation and the total time of the simulation obtained as the sum of the t_{ij} *values* , respectively.

Supporting Information
Supporting Information is available from the Wiley Online Library or from the author.

Acknowledgements
The authors acknowledge funding support from Department of Energy, Bridging Research Interactions through collaborative Development Grants in Energy (BRIDGE) program under contract DE-FOA-0000654-1588, from the Walloon Region (WCS Project N° 1117306), from the European Commission / Walloon Region (FEDER – Smartfilm RF project), from the Interuniversity Attraction Pole program of the Belgian Federal Science Policy Office (PAI 7/05), from the Programme d'Excellence de la Région Wallonne (OPTI2MAT project), from

the Belgian National Fund for Scientific Research (FNRS - Project N° 2.4565.11), from a concerted research action of the French Community of Belgium (ARC Project N° 20061) and from the National Science Foundation Division of Materials Research Solid-State Chemistry Program (DMR-1303178). Y. G. benefits from a mandate of Francqui Research Professor. G. S. kindly acknowledges postdoctoral fellowship support from the David and Alice van Buuren Funds of the Belgian American Educational Foundation (B.A.E.F.) and from the Fulbright Foundation (Fulbright Research Scholar Fellow). J.C. is a FNRS Research Director.

Received: ((will be filled in by the editorial staff))
Revised: ((will be filled in by the editorial staff))
Published online: ((will be filled in by the editorial staff))

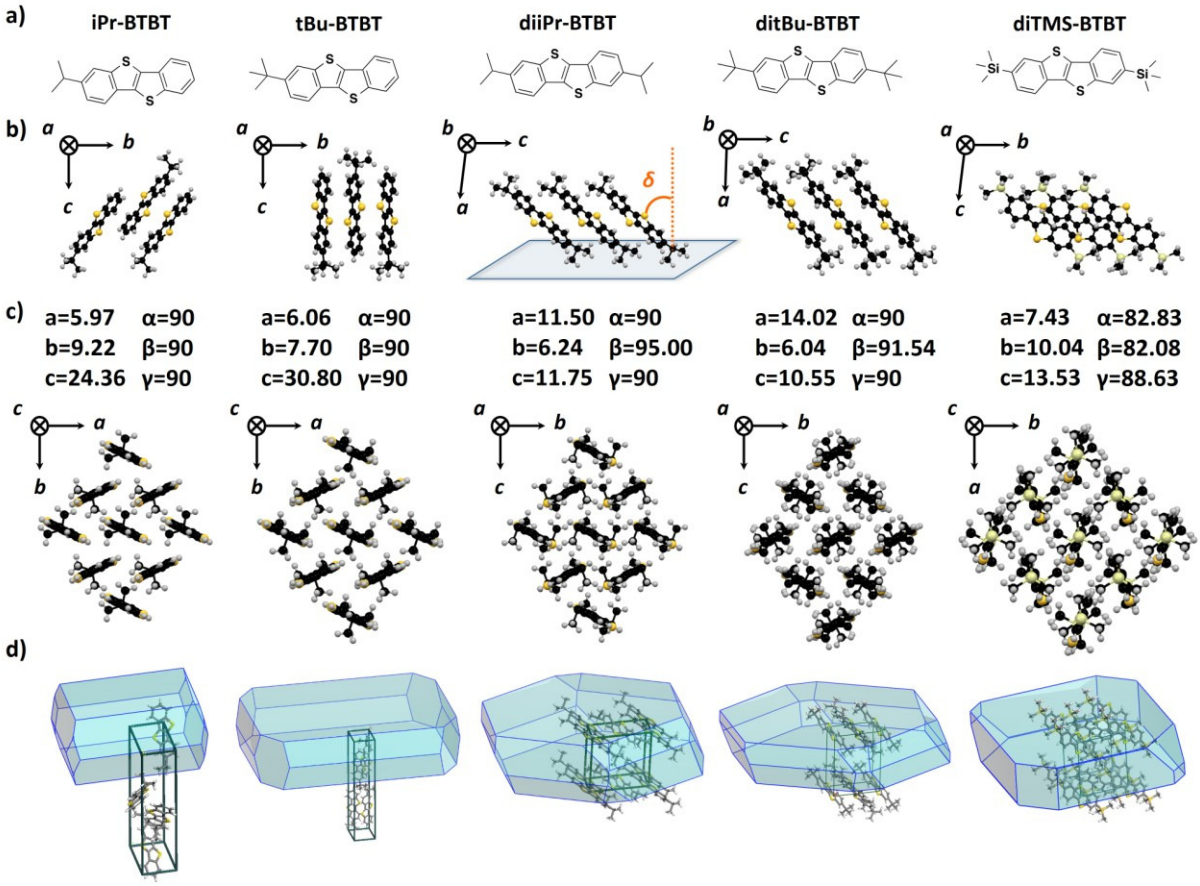

Figure 1. a) Molecular structure of the different bulky end-capped BTBTs classified by ascending order of bulkiness. b) Side view of the lamellar herringbone packing structure. Terminal substitution determines the in-plane tilt (δ) of the BTBT cores, with **diTMS-BTBT** (51.3°) > [**diiPr-BTBT** (42.5°) - **iPr-BTBT** (35.8°)] > [**ditBu-BTBT** (40.5°) - **tBu-BTBT** (0°)]. c) Lattice parameters and top view of the lamellar herringbone packing structure. d) Calculated crystal growth morphology of the different BTBTs.

a)

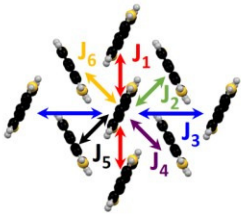

Compound	J_1 [meV]	J_2 [meV]	J_3 [meV]	J_4 [meV]	J_5 [meV]	J_6 [meV]
iPr-BTBT	58	11	0.3	11	21	21
tBu-BTBT	35	14	0.4	16	16	14
diiPr-BTBT	57	35	0.2	35	35	35
ditBu-BTBT	60	53	0.2	53	53	53
diTMS-BTBT	2	43	1	37	43	37

b)

Compound	Ionization potential [eV]	λ_+ [eV]	μ_{max} [$cm^2 V^{-1} s^{-1}$]	μ [$cm^2 V^{-1} s^{-1}$]	V_{th} (V)	I_{on}/I_{off}
iPr-BTBT	5.8	0.24	0.08	0.04±0.04	-100.0±15.6	$2.1\ 10^5$
tBu-BTBT	5.5	0.24	2.1	0.4±0.6	-68.5±5.5	$1.6\ 10^7$
diiPr-BTBT	5.6	0.24	/	/	/	/
ditBu-BTBT	5.7	0.25	17.0	7.1±4.0	-71.0±5.7	$3.0\ 10^9$
diTMS-BTBT	5.6	0.29	0.6	0.3±0.1	-88.2±7.4	$1.0\ 10^7$

Figure 2. a) Top view of the lamellar herringbone packing structure with DFT-calculated transfer integrals. b) Performances of PVT grown single crystals of the different BTBT derivatives extracted from 3, 10, 5, 42 and 5 devices respectively.

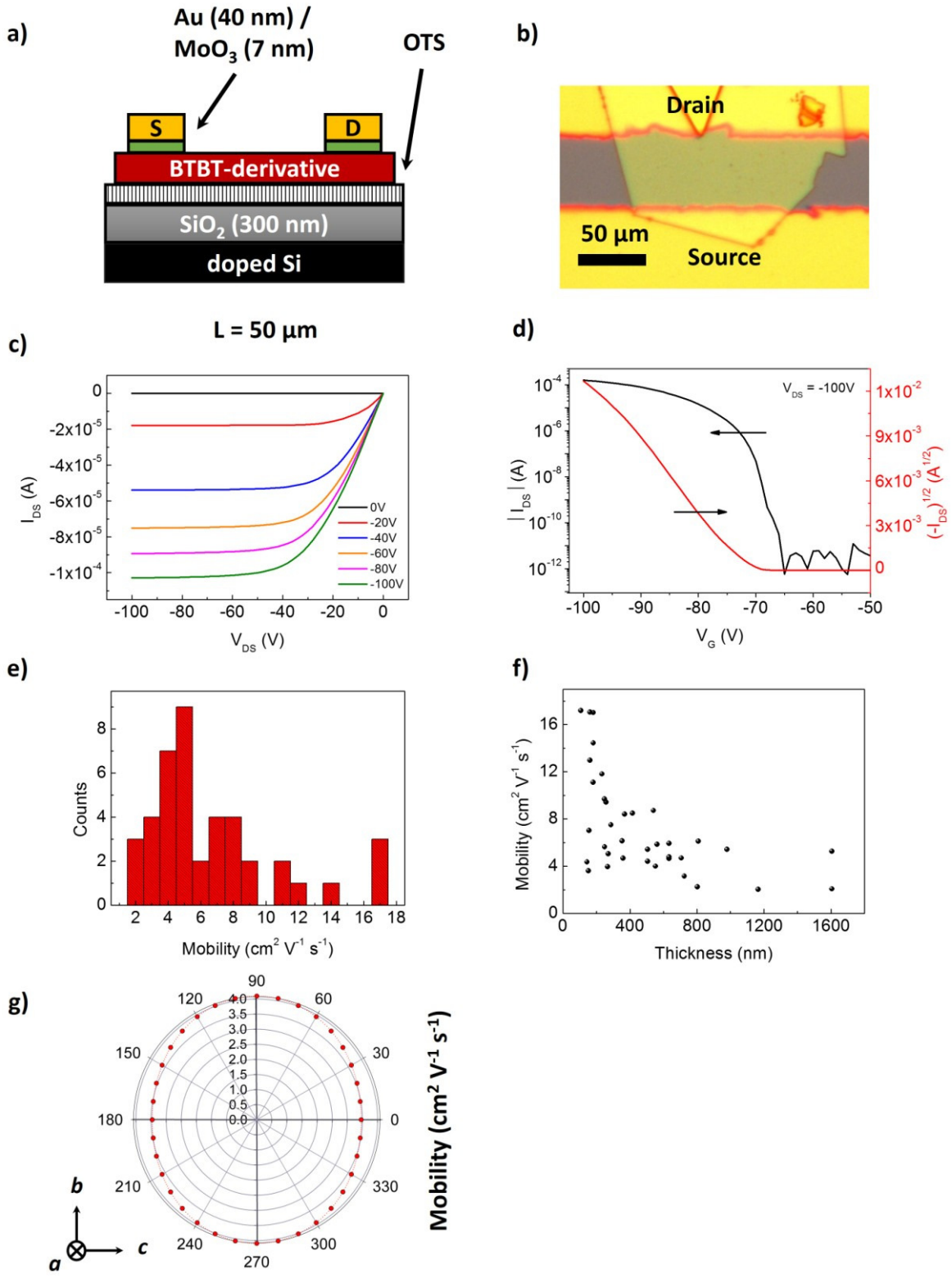

Figure 3. a) Schematic of the bottom-gate top-contact single crystal device structure (not to scale). b) Optical micrograph of a **ditBu-BTBT** device presenting a channel width of 124 µm. c), d) output and transfer (in the saturation regime) characteristics of the depicted device presenting a field-effect mobility of 17 $cm^2 V^{-1} s^{-1}$. e) Mobility histogram of the 42 **ditBu-BTBT** devices. f) Thickness dependence of the field-effect mobility. g) Calculated field-effect mobility anisotropy as a function of the crystallographic orientation for **ditBu-BTBT**.

A series of bulky end-capped [1]benzothieno[3,2-b]benzothiophenes (BTBTs) have been developed in order to tune the packing structure via terminal substitution. A coupled theoretical and experimental study allowed us to identify 2,7-di-*tert*-butylBTBT as a new high-performance organic semiconductor with large and well-balanced transfer integrals as evidenced by quantum-chemical calculations. Single-crystal FETs showed a remarkable saturation mobility as high as 17 $cm^2 V^{-1} s^{-1}$.

Keyword: organic semiconductor; single crystal; high mobility; organic transistor

Guillaume Schweicher, Vincent Lemaur, Claude Niebel, Christian Ruzié, Ying Diao, Osamu Goto, Wen-Ya Lee, Yeongin Kim, Jean-Baptiste Arlin, Jolanta Karpinska, Alan R. Kennedy, Sean R. Parkin, Yoann Olivier, Stefan C. B. Mannsfeld, Jérôme Cornil, Yves H. Geerts*, Zhenan Bao*

Bulky End-Capped [1]Benzothieno[3,2-*b*]benzothiophenes: Reaching High Mobility Organic Semiconductors by Fine Tuning of the Crystalline Solid-State Order

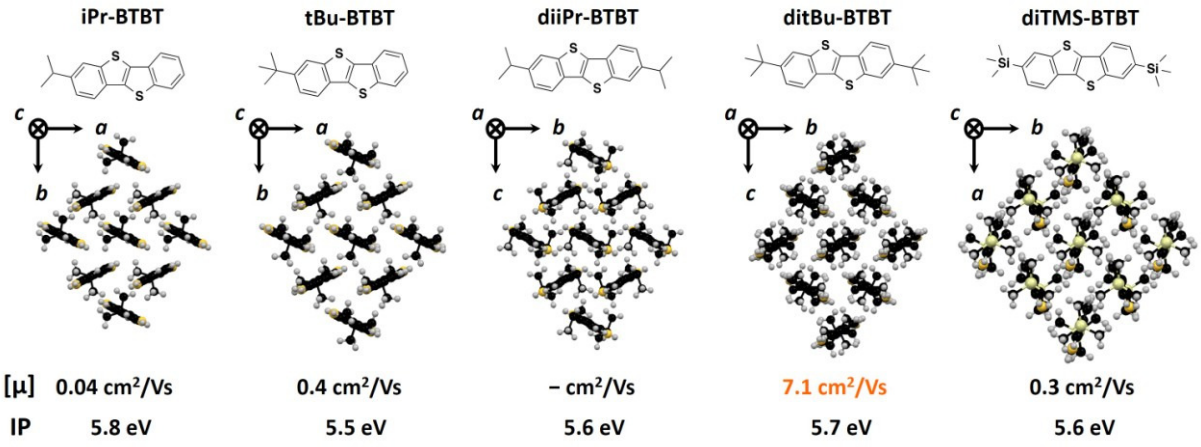

Supporting Information

Bulky End-Capped [1]Benzothieno[3,2-*b*]benzothiophenes: Reaching High Mobility Organic Semiconductors by Fine Tuning of the Crystalline Solid-State Order

Guillaume Schweicher, Vincent Lemaur, Claude Niebel, Christian Ruzié, Ying Diao, Osamu Goto, Wen-Ya Lee, Yeongin Kim, Jean-Baptiste Arlin, Jolanta Karpinska, Alan R. Kennedy, Sean R. Parkin, Yoann Olivier, Stefan C. B. Mannsfeld, Jérôme Cornil, Yves H. Geerts, Zhenan Bao**

1. General

Reagents and Starting Materials

All reagents and solvents were purchased from Aldrich, Alfa Aesar, or Acros. The reagents - [1]benzothieno[3,2-*b*][1]benzothiophene (**BTBT**), [S1] 2,7-diiodo-[1]benzothieno[3,2-*b*][1]benzothiophene (**diI-BTBT**),[S2] ([1]benzothieno[3,2-*b*][1]benzothien-2-yl)ethan-1-one, [S3] and 1,1'-([1]benzothieno[3,2-*b*][1]benzothien-2,7-diyl)bis(ethan-1-one) [S3] were synthesized according to known procedures.

Synthesis and Characterization

All the reactions were carried out under an argon atmosphere. Air- and/or moisture-sensitive liquids and solutions were transferred via a syringe or a Teflon cannula. Analytical thin-layer chromatography (TLC) was performed on aluminium plates with 10-12 μm silica gel containing a fluorescent indicator (Merck silica gel 60 F254). TLC plates were visualized by exposure to ultraviolet light (254 nm and 365 nm). Flash column chromatography was performed on Grace Davisil LC60A (70-200μm) silica. All NMR spectra were recorded on Bruker Avance 300 spectrometer. Chemical shifts are reported in parts per million (ppm, δ scale) from tetramethylsilane for ^{1}H NMR (δ 0 ppm in chloroform) and from the solvent carbon for ^{13}C NMR (e.g., δ 77.16 ppm for chloroform). The data are presented in the following format: chemical shift, multiplicity (s = singlet, d = doublet, t = triplet, m = multiplet), coupling constant in hertz (Hz), signal area integration in natural numbers, assignment (italic). Mass spectra were measured on a Waters Autospec 6F EI+ mass spectrometer. Melting points were obtained on a Mettler Toledo FP80 Melting Point System with FP82 hot plate.

2. Synthesis

Experimental Section

The syntheses of **ditBu-BTBT**, **tBu-BTBT**, **iPr-BTBT** and **diiPr-BTBT** were carried out starting from **BTBT**[S1]. Synthesis of **diTMS-BTBT** was carried out from **diI-BTBT**[S2]. All the target molecules were characterized by melting point (m.p.), ^{1}H NMR, ^{13}C NMR, and mass spectroscopy.

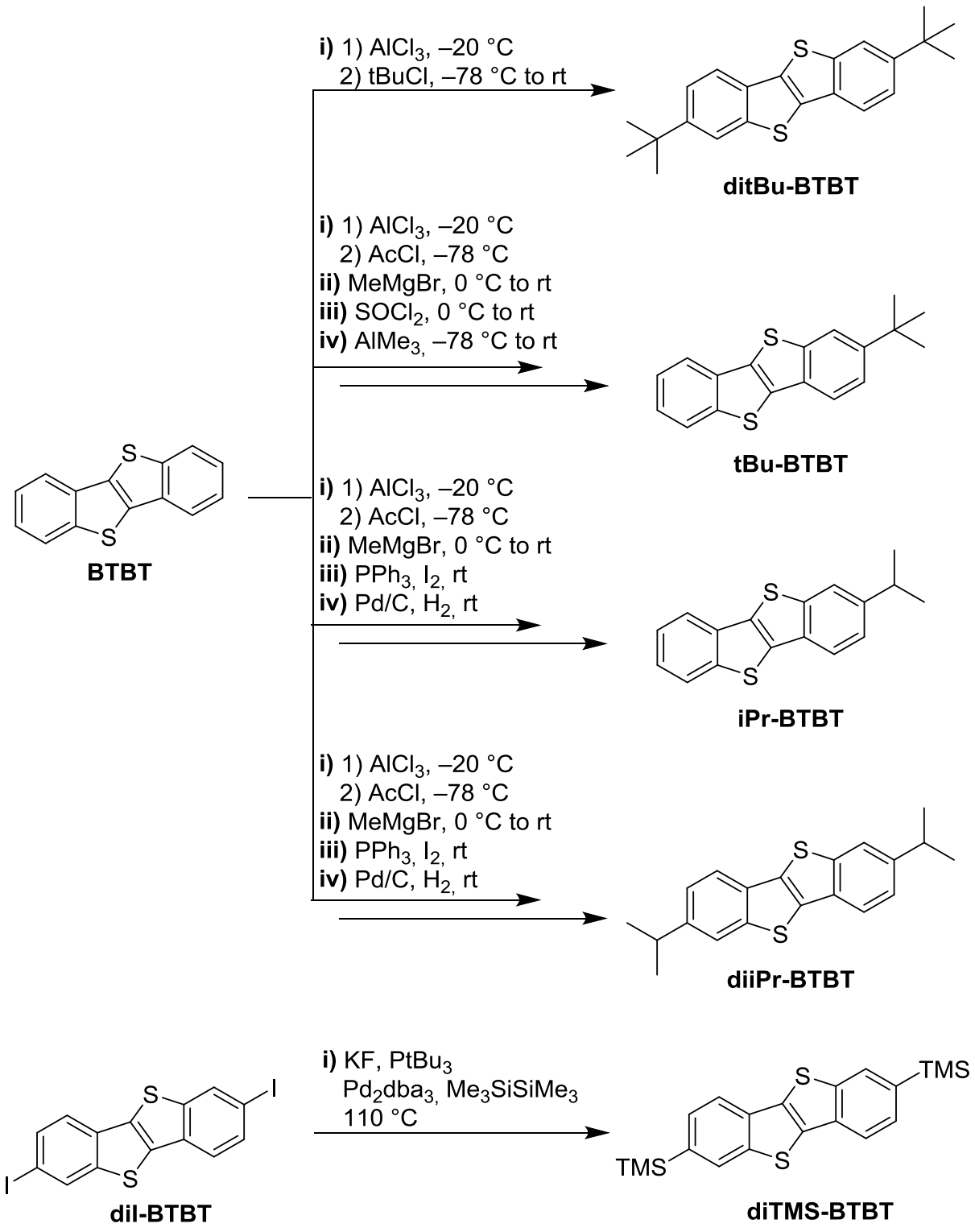
i) 1) AlCl3, –20 °C
2) tBuCl, –78 °C to rt
ditBu-BTBT
i) 1) AlCl3, –20 °C
2) AcCl, –78 °C
ii) MeMgBr, 0 °C to rt
iii) SOCl2, 0 °C to rt
iv) AlMe3, –78 °C to rt
tBu-BTBT
BTBT
i) 1) AlCl3, –20 °C
2) AcCl, –78 °C
ii) MeMgBr, 0 °C to rt
iii) PPh3, I2, rt
iv) Pd/C, H2, rt
iPr-BTBT
i) 1) AlCl3, –20 °C
2) AcCl, –78 °C
ii) MeMgBr, 0 °C to rt
iii) PPh3, I2, rt
iv) Pd/C, H2, rt
diiPr-BTBT
diI-BTBT
i) KF, PtBu3
Pd2dba3, Me3SiSiMe3
110 °C
diTMS-BTBT

Synthesis of **ditBu-BTBT**

The **ditBu-BTBT** was synthetized by a Friedel-Crafts alkylation using the conditions of diacylation of **BTBT**[S3] with $AlCl_3$ as Lewis acid.

2,7-Di-*tert*-butyl-[1]benzothieno[3,2-*b*][1]benzothiophene (**ditBu-BTBT**)

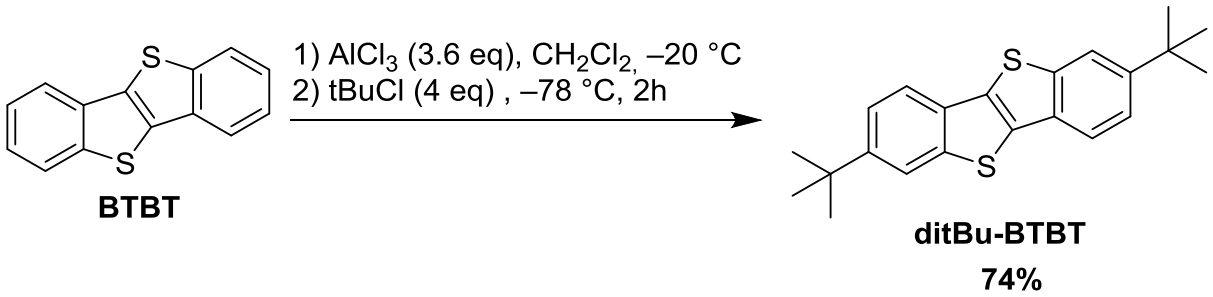

To a solution of [1]benzothieno[3,2-*b*][1]thiophene **BTBT** (2.00 g, 8.32 mmol) in dry CH_2Cl_2 (150 mL) was added $AlCl_3$ (3.99 g, 29.96 mmol) in one portion, at –20 °C and under an argon atmosphere. The reaction mixture was cooled down to –78 °C. *tert*-Butyl chloride (3.64 mL, 33.29 mmol) was then added dropwise in about 30 min. The reaction mixture was stirred further at –78 °C for 2h. The reaction was quenched by the addition of ice/water (100 mL). Volatiles were removed under reduced pressure. The formed precipitate was isolated by filtration, washed with water (3x50 mL) and methanol (3x50 mL) and finally dried to afford a white powder. Further recrystallization in heptane afforded a white crystalline powder (2.17 g, 74 %). m.p.: 275-277 °C; ^{1}H NMR (300 MHz, $CDCl_3$, 25°C, TMS) δ = 7.90 (d, ^4J(H,H) = 1.0 Hz, 2 H, CH), 7.80 (d, ^3J(H,H) = 8.3 Hz, 2 H, CH), 7.50 (dd, ^3J(H,H) = 8.3 Hz and ^4J(H,H) = 1 Hz, 2 H, CH), 1.42 (s, 18 H, CH_3); ^{13}C NMR (75 MHz, $CDCl_3$, 25°C) δ = 148.3 (C), 142.4 (C), 132.7 (C), 130.9 (C), 123.0 (CH), 120.9 (CH), 120.2 (CH), 35.1 (C), 31.5(CH_3); EI–HRMS: Calc for $C_{22}H_{24}S_2$ [$M^{+\cdot}$]: 352.1319. Found: 352.1305.

Synthesis of **tBu-BTBT**

The **tBu-BTBT** was synthetized by a four steps reaction. Starting from **BTBT**, acylation was carried out by a Friedel-Crafts reaction using the conditions of mono-acetylation [S3], followed by a methylation reaction with methylmagnesium bromide to afford the isopropanol derivative. Chlorination of the alcohol by thionyl chloride followed by an alkylation with trimethyl aluminium afforded **tBu-BTBT**.

2-([1]Benzothieno[3,2-*b*][1]benzothien-2-yl)propan-2-ol

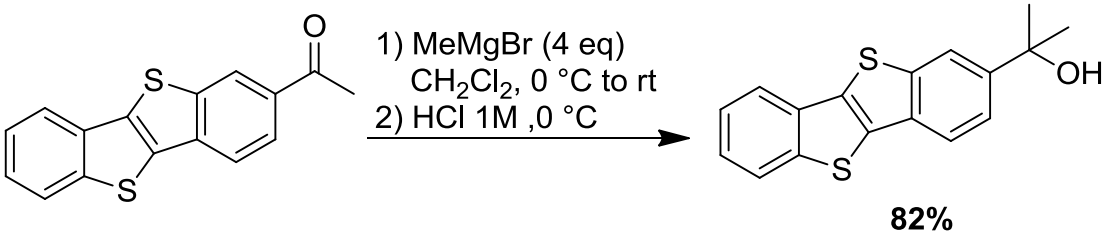

82%

To a solution of ([1]benzothieno[3,2-*b*][1]benzothien-2-yl)ethan-1-one (4.89 g, 17.32 mmol) in dry CH_2Cl_2 (500 mL) was added MeMgBr (3M in Et_2O, 22.9 mL, 68.79 mmol) over 45 min at 0 °C under an argon atmosphere. The mixture was stirred and allowed to warm to room temperature. After 1 h at room temperature, the reaction mixture was cooled down to 0 °C, and was quenched by the addition of HCl 1M (100 mL). The organic layer was separated, washed with water, dried over $MgSO_4$, and concentrated under vacuum. The resulting residue was subjected to column chromatography (silica, hot hexanes) to afford a white powder (4.19 g, 82 %). m.p.: 178-180 °C; ^{1}H NMR (300 MHz, $CDCl_3$, 25°C, TMS) δ = 8.07 (dd, ^4J(H,H) = 1.6 Hz and ^5J(H,H) = 0.5 Hz, 1 H, CH), 7.94-7.85 (m, 2 H, CH), 7.84 (dd, ^3J(H,H) = 8.4 Hz and ^5J(H,H) = 0.5 Hz, 1 H, CH), 7.56 (dd, ^3J(H,H) = 8.4 Hz and ^4J(H,H) = 1.6 Hz, 1 H, CH), 7.49-7.35 (m, 2 H, CH), 1.87 (s, 1 H, OH), 1.68 (s, 6 H, CH_3); ^{13}C NMR (75 MHz, $CDCl_3$, 25°C) δ = 146.4 (C), 142.5 (C), 142.2 (C), 133.4 (C), 133.1 (C), 133.1 (C), 131.7 (C), 124.9 (CH), 124.8 (CH), 124.0 (CH), 122.0 (CH), 121.5 (CH), 121.3 (CH), 119.7 (CH), 72.8 (C-OH), 32.0 (CH_3).; EI–HRMS: Calc for $C_{17}H_{14}OS_2$ [$M^{+\cdot}$]: 298.0486. Found: 298.0489.

2-*tert*-Butyl-[1]benzothieno[3,2-*b*][1]benzothiophene (**tBu-BTBT**)

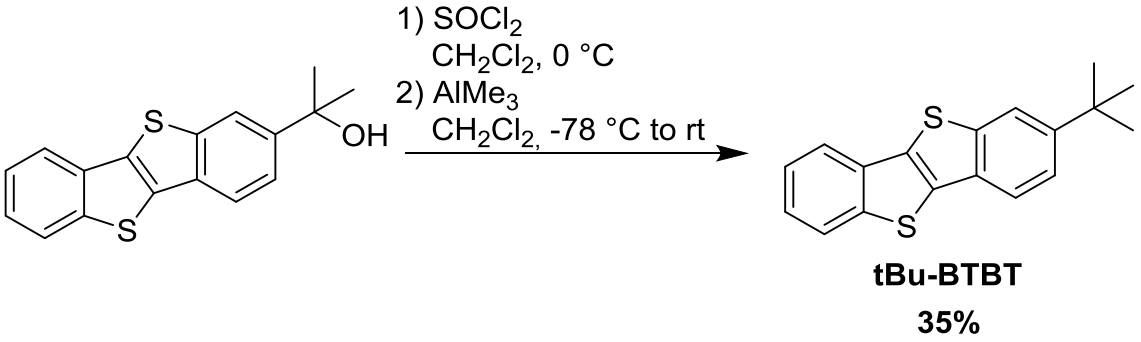

tBu-BTBT

35%

To a solution of 2-([1]benzothieno[3,2-*b*][1]benzothien-2-yl)propan-2-ol (2.00 g, 6.70 mmol) in dry $CHCl_3$ (300 mL), cooled down to 0 °C, was added dropwise $SOCl_2$ (2.44 mL, 33.51 mmol). The mixture was stirred at 0 °C for 2 h. The reaction mixture was then warmed up to room temperature and volatiles (remaining $SOCl_2$ and $CHCl_3$) were removed under reduced pressure. The residue was diluted with dry CH_2Cl_2 (500 mL), before being cooled down to -78°C. Trimethyl aluminium (6.70 mL, 13.40 mmol) was then added dropwise at this temperature, and the reaction mixture was allowed to warm up to room temperature overnight. The reaction mixture was quenched by the addition of HCl 1M (100 mL). The organic layer was separated, washed with water, dried over $MgSO_4$, and concentrated under vacuum. The resulting residue was subjected to column chromatography (silica, hot hexanes) to afford a white powder (0.703 g, 35 %). m.p.: 170-172 °C; ^{1}H NMR (300 MHz, $CDCl_3$, 25°C, TMS) δ = 7.93-7.85 (m, 3 H, CH), 7.81 (dd, ^3J(H,H) = 8.4 Hz and ^5J(H,H) = 0.5 Hz, 1 H, CH), 7.51 (dd, ^3J(H,H) = 8.4 Hz and ^4J(H,H) = 1.7 Hz, 1 H, CH),7.48-7.34 (m, 2 H, CH), 1.42 (s, 9 H, CH_3); ^{13}C NMR (75 MHz, $CDCl_3$, 25°C) δ = 148.6 (C), 142.6 (C), 142.1 (C), 133.3 (C), 133.2 (C), 132.8 (C), 130.7 (C), 124.8 (CH), 124.7 (CH), 124.0 (CH), 123.1 (CH), 121.4 (CH), 121.1 (CH), 120.3 (CH), 35.1 (C), 31.5 (CH_3); EI–HRMS: Calc for $C_{18}H_{16}S_2$ [$M^{+\cdot}$]: 296.0693. Found: 296.0689.

Synthesis of **iPr-BTBT**

The **iPr-BTBT** was synthetized by a two steps reaction. Starting from 2-([1]benzothieno[3,2-*b*][1]benzothien-2-yl)propan-2-ol, reaction with triphenyl diiodide[S4] afforded a mixture of **iPr-BTBT** and elimination product. The mixture was subjected to palladium catalytic hydrogenation to **iPr-BTBT**.

2-*iso*-Propyl-[1]benzothieno[3,2-*b*][1]benzothiophene (**iPr-BTBT**)

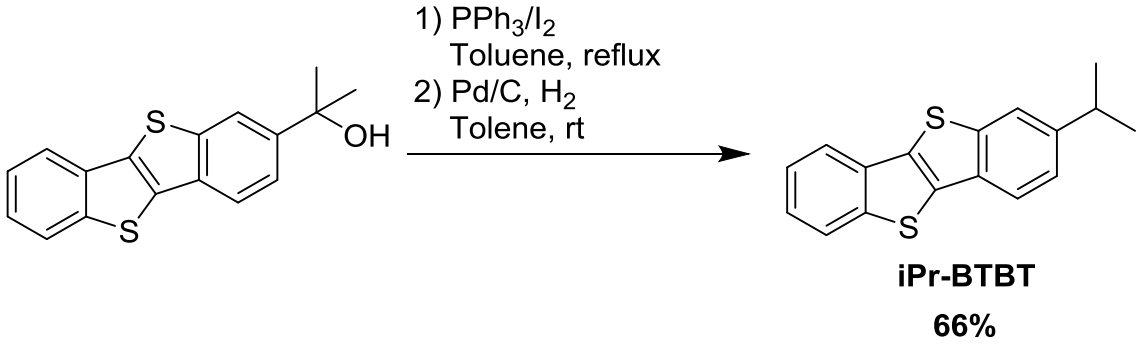

To a solution of 2-([1]benzothieno[3,2-*b*][1]benzothien-2-yl)propan-2-ol (1.01 g, 3.20 mmol) in anhydrous toluene (50 mL) was added PPh_3 (1.01 g, 3.80 mmol) and iodine (0.98 g, 3.80 mmol). The mixture was stirred at reflux for 2 h until disappearance of starting materials. The reaction mixture was cooled down to rt, and then was quenched by the addition of 5% aqueous Na_2SO_5 (50 mL). The organic layer was separated, washed with water, dried over $MgSO_4$, and concentrated under vacuum. The resulting residue (630 mg) containing a mixture of **iPr-BTBT** and elimination product was subjected to palladium catalytic hydrogenation with Pd (10% on carbon, 31 mg) under H_2 (1 atm). The mixture was stirred overnight, filtered on Celite, and concentrated under vacuum. The resulting residue was subjected to column chromatography (silica, hot hexanes) to afford a white crystalline powder (626 mg, 66 %). m.p.: 175-177 °C; ^{1}H NMR (300 MHz, $CDCl_3$, 25°C, TMS) δ = 7.94-7.83 (m, 2 H, CH), 7.80 (d, ^3J(H,H) = 8.3 Hz, 1 H, CH), 7.76 (d, ^4J(H,H) = 1.0 Hz, 1 H, CH),7.49-7.34 (m, 2 H, CH), 7.33 (dd, ^3J(H,H) = 8.3 Hz and ^4J(H,H) = 1.0 Hz, 1 H, CH), 3.07 (hept, ^3J(H,H) = 6.9 Hz, 1 H,

CH), 1.34 (d, ^{3}J(H,H) = 6.9 Hz, 6 H, CH_3); ^{13}C NMR (75 MHz, $CDCl_3$, 25°C) δ = 146.3 (C), 142.6 (C), 142.1 (C), 133.3 (C), 133.2 (C), 132.7 (C), 131.2 (C), 124.8 (CH), 124.7 (CH), 124.1 (CH), 124.0 (CH), 121.41 (CH), 121.36 (CH), 120.34 (CH), 34.4 (C), 24.2 (CH_3); EI–HRMS: Calc for $C_{17}H_{14}S_2$ [$M^{+\cdot}$]: 282.0537. Found: 282.0548.

Synthesis of **diiPr-BTBT**

The **diiPr-BTBT** was synthetized by a four steps reaction. Starting from BTBT, acylation was carried out by a Friedel-Crafts reaction using the conditions of di-acetylation [S3], followed by a methylation reaction with methylmagnesium bromide to afforded the isopropanol derivative. 2,2'-([1]benzothieno[3,2-*b*][1]benzothien-2,7-diyl)bis(propan-2-ol) was subjected to reaction with triphenyl diiodide[S4] to afford a mixture of **diiPr-BTBT** and elimination product, and finally the mixture was subjected to palladium catalytic hydrogenation to **diiPr-BTBT**.

2,2'-([1]Benzothieno[3,2-*b*][1]benzothien-2,7-diyl)bis(propan-2-ol)

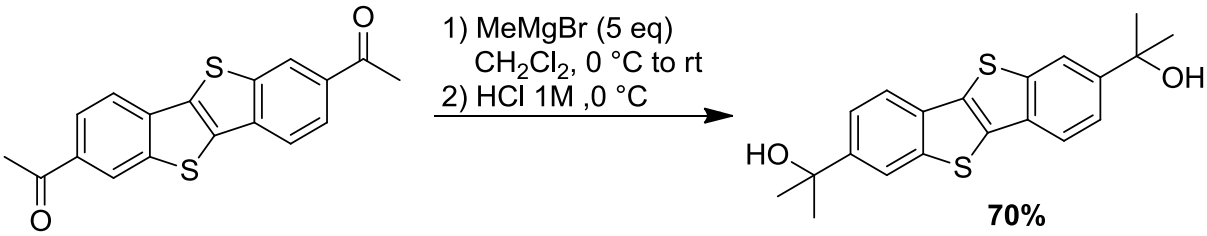

To a solution of 1,1'-([1]benzothieno[3,2-*b*][1]benzothien-2,7-diyl)bis(ethan-1-one) (1.34 g, 4.10 mmol) in dry CH_2Cl_2 (800 mL) was added MeMgBr (3M in Et_2O, 6.88 mL, 20.6 mmol) over 45 min at 0 °C under an argon atmosphere. The mixture was stirred and allowed to warm to room temperature. After one night at room temperature, the reaction mixture was cooled down to 0 °C, and then was quenched by the addition of HCl 1M (200 mL). The organic layer was separated, washed with water, dried over $MgSO_4$, and concentrated under vacuum. The resulting residue was triturated in chloroform and filtrated to afford a white powder (1.02 g, 70 %). m.p.: 216-218 °C; ^{1}H NMR (300 MHz, $CDCl_3$, 25°C, TMS) δ = 8.08 (dd, ^{4}J(H,H) =

1.7 Hz and ^{5}J(H,H) = 0.6 Hz, 2 H, CH), 7.84 (dd, ^{3}J(H,H) = 8.4 Hz and ^{5}J(H,H) = 0.6 Hz, 2 H, CH), 7.57 (dd, ^{3}J(H,H) = 8.4 Hz and ^{4}J(H,H) = 1.7 Hz, 2 H, CH), 1.86 (s, 2 H, OH), 1.69 (s, 12 H, CH_3); ^{13}C NMR (75 MHz, $CDCl_3$, 25°C) δ = 146.5 (C), 142.6 (C), 133.3 (C), 132.00 (C), 122.2 (CH), 121.4 (CH), 119.8 (CH), 73.0 (C-OH), 32.2 (CH_3).; EI–HRMS: Calc for $C_{20}H_{20}O_2S_2$ [$M^{+\cdot}$]: 356.0905. Found: 356.0913.

2,7-Di-*iso*-propyl-[1]benzothieno[3,2-*b*][1]benzothiophene (**diiPr-BTBT**)

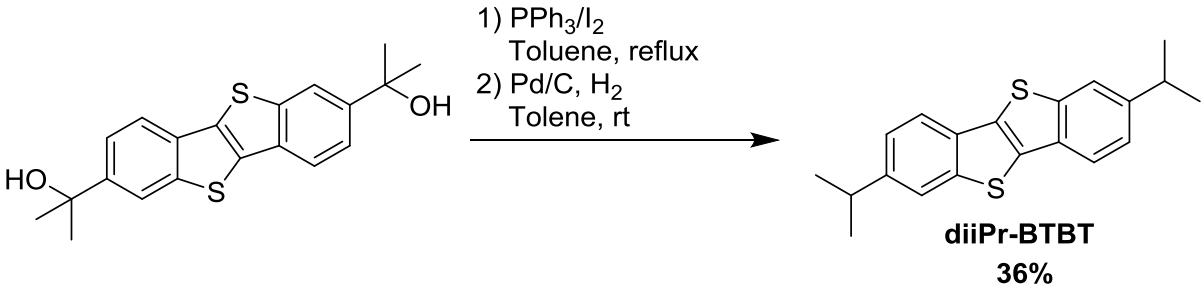

To a solution of 2,2'-([1]benzothieno[3,2-*b*][1]benzothien-2,7-diyl)bis(propan-2-ol) (808 mg, 2.26 mmol) in anhydrous toluene (50 mL) was added PPh_3 (1.49 g, 5.60 mmol) and iodine (1.44 g, 5.60 mmol). The mixture was stirred at reflux for 2 h until disappearance of starting materials. The reaction mixture was cooled down to rt, and then was quenched by the addition of 5% aqueous Na_2SO_5 (50 mL). The organic layer was separated, washed with water, dried over $MgSO_4$, and concentrated under vacuum. The resulting residue (790 mg) containing a mixture of **diiPr-BTBT** and elimination product was subjected to palladium catalytic hydrogenation with Pd (10% on carbon, 10 mg) under H_2 (1 atm). The mixture was stirred overnight, filtered on Celite, and concentrated under vacuum. The resulting residue was subjected to column chromatography (silica, hot hexanes) to afford a white crystalline powder (260 mg, 36 %). m.p.: 196-198 °C; ^{1}H NMR (300 MHz, $CDCl_3$, 25°C, TMS) δ = 7.80 (d, ^{3}J(H,H) = 8.2 Hz, 2 H, CH), 7.75 (d, ^{4}J(H,H) = 1.2 Hz, 2 H, CH), 7.33 (dd, ^{3}J(H,H) = 8.2 Hz and ^{4}J(H,H) = 1.2 Hz, 2 H, CH), 3.07 (hept, ^{3}J(H,H) = 6.9 Hz, 2 H, CH), 1.34 (d, ^{3}J(H,H) = 6.9 Hz, 12 H, CH_3); ^{13}C NMR (75 MHz, $CDCl_3$, 25°C) δ = 146.2 (C), 142.6 (C), 132.7 (C),

131.5 (C), 124.2 (CH), 121.5 (CH), 121.3 (CH), 34.5 (CH), 24.3 (CH_3); EI–HRMS: Calc for $C_{20}H_{20}S_2$ [$M^{+\cdot}$]: 324.1006. Found: 324.1001.

Synthesis of di**TMS-BTBT**

The **diTMS-BTBT** was synthetized by a palladium-catalyzed silylation[S5] of 2,7-diiodo-[1]benzothieno[3,2-*b*][1]benzothiophene[S6] with hexamethyldisilane.

2,7-Di-trimethylsilyl-[1]benzothieno[3,2-*b*][1]benzothiophene

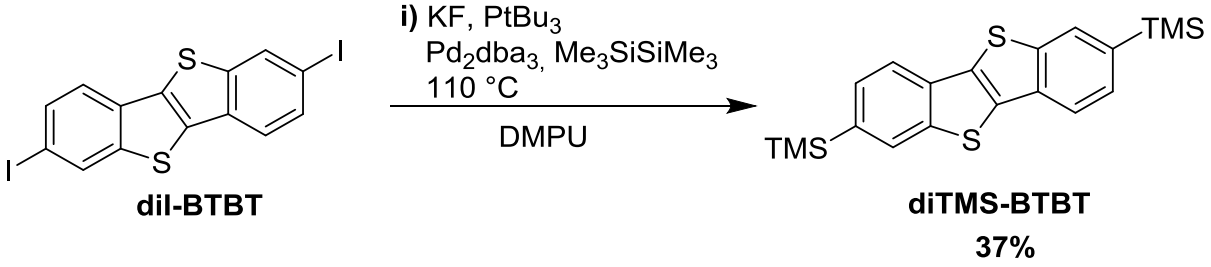

A mixture of 2,7-diiodo-[1]benzothieno[3,2-*b*][1]benzothiophene) (**diI-BTBT**) (986 mg, 2 mmol), anhydrous KF (929 mg, 16 mmol), tri-*tert*-butylphosphine (97 µL, 0.4 mmol), and hexamethyldisilane (1.64 mL, 8 mmol) was dried under vacuum for 5 min. 1,3-Dimethyl-3,4,5,6-tetrahydro-2(1H)-pyrimidinone (40 mL) was added, and the mixture was degassed by 2 "freeze-pump-thaw" cycles. $Pd_2(dba)_3$•$CHCl_3$ (dba = dibenzylideneacetone) (183 mg, 0.4 mmol) was added, and the mixture was degassed by one more "freeze-pump-thaw" cycle. After refilling with argon. The sealed schlenk flask was placed on a preheated hot plate and heated for 2 days at 110 °C. After cooling to room temperature, water was added, and the suspension filtrated. The solid was washed with water (3x50 mL) and MeOH (2x50 mL). After drying, the resulting residue was subjected to column chromatography (silica, hot hexanes) to afford a white crystalline powder (284 mg, 37 %).m.p.: 214-216 °C; ^{1}H NMR (300 MHz, $CDCl_3$, 25°C, TMS) δ = 8.06 (dd, ^4J(H,H) = 0.8 Hz and ^5J(H,H) = 0.5 Hz, 2 H, CH), 7.88 (dd, ^3J(H,H) = 7.8 Hz and ^5J(H,H) = 0.5 Hz, 2 H, CH), 7.58 (dd, ^3J(H,H) = 7.8 Hz

and ^{4}J(H,H) = 0.8 Hz, 2 H, CH), 0.35 (s, 18 H, CH_3); ^{13}C NMR (75 MHz, $CDCl_3$, 25°C) δ = 142.1 (C), 137.3 (C), 133.7 (C), 133.3 (C), 129.4 (CH), 128.9 (CH), 121.0 (CH), 0.96 (CH_3); EI–HRMS: Calc for $C_{20}H_{24}Si_2S_2$ [$M^{+\cdot}$]: 384.0858. Found: 384.0860.

[S1] M. Saito, I. Osaka, E. Miyazaki, K. Takimiya, H. Kuwabara, M. Ikeda, *Tetrahedron Lett.* **2011**, *52*, 285.

[S2] K. Takimiya, H. Ebata, K. Sakamoto, T. Izawa, T. Otsubo, Y. Kunugi, *J. Am. Chem. Soc.* **2006**, *128*, 12604.

[S3] B. Košata, V. Kozmík, J. Svoboda, *Collect. Czech. Chem. Commun.* **2002**, *67*, 645.

[S4] I. Furukawa, B. Zhou, S. Hashimoto, *Nippon Kagaku Kaishi* **1984**, *1984*, 1208.

[S5] T. Iwasawa, T. Komano, A. Tajima, M. Tokunaga, Y. Obora, T. Fujihara, Y. Tsuji, *Organometallics* **2006**, *25*, 4665.

[S6] H. Ebata, T. Izawa, E. Miyazaki, K. Takimiya, M. Ikeda, H. Kuwabara, T. Yui, *J. Am. Chem. Soc.* **2007**, *129*, 15732.

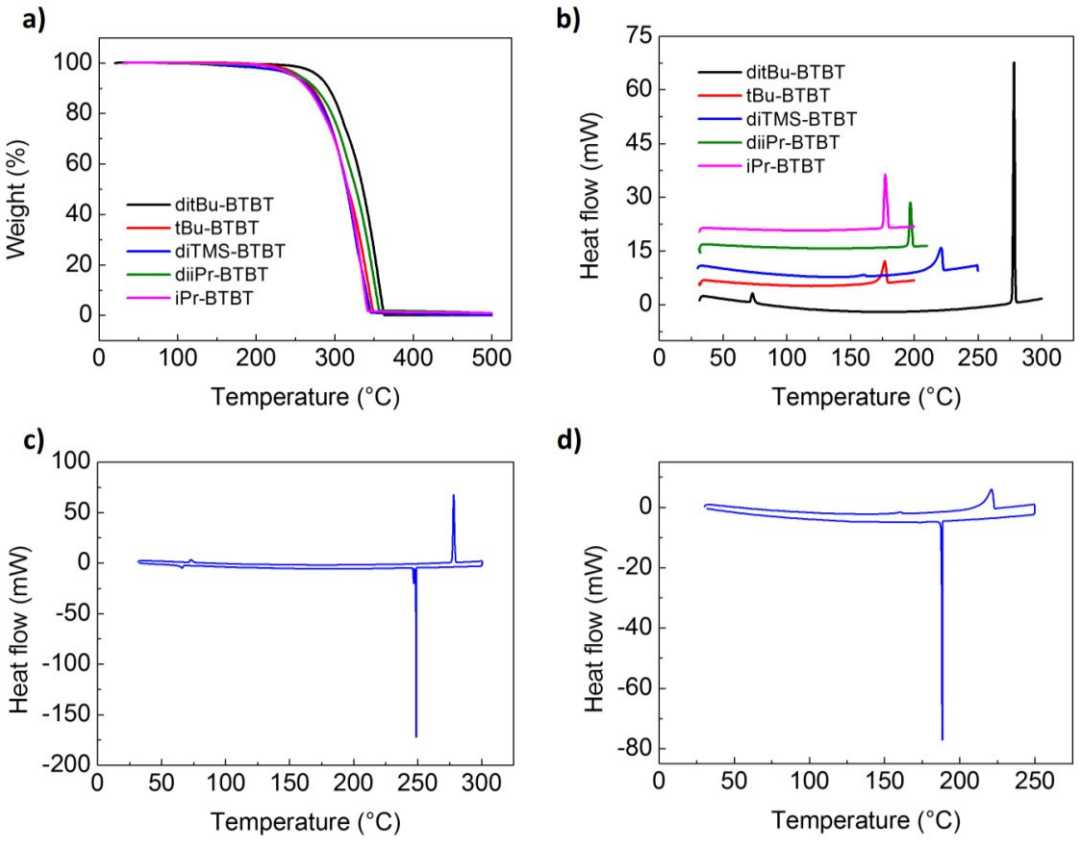

Figure S1. a) TGA and b) DSC traces of the bulky end-capped BTBTs recorded at 10 °C min^{-1}. Complete DSC trace of c) **ditBu-BTBT** and d) **diTMS-BTBT** highlighting the reversible nature of the crystal-crystal transition.

Table S1. DSC transition temperatures and associated energies.

Compound	$T_{C\rightarrow C}$ [°C][a)]	$\Delta H_{C\rightarrow C}$ [kJ/mol]	$T_{C\rightarrow I}$ [°C]	$\Delta H_{C\rightarrow I}$ [kJ/mol]
iPr-BTBT	-	-	175.7	28.2
tBu-BTBT	-	-	172.8	21.0
diiPr-BTBT	-	-	195.6	24.6
ditBu-BTBT	71.2	3.1	277.1	38.2
diTMS-BTBT	154.7	1.1	215.3	29.1

[a)] C: Crystal phase, I: Isotropic phase

Table S2. PVT growth conditions of the different BTBT derivatives.

Compound	Growth time [min]	Sublimation zone temperature [°C]	Growth zone temperature [°C]
iPr-BTBT	150	180	90
tBu-BTBT	120	230	120
diiPr-BTBT	180	230	110
ditBu-BTBT	30 to 90	215	190
diTMS-BTBT	30 to 40	200	90

Table S3. Crystal data for the bulky end-capped BTBTs.

	iPr-BTBT	**tBu-BTBT**	**diiPr-BTBT**	**ditBu-BTBT**	**diTMS-BTBT**
Empirical formula	$C_{17}H_{14}S_2$	$C_{18}H_{16}S_2$	$C_{20}H_{20}S_2$	$C_{22}H_{24}S_2$	$C_{20}H_{24}S_2Si_2$
Formula weight	282.40	296.43	324.48	352.53	384.69
Temperature (K)	90.0(2)	90.0(2)	90.0(2)	123(2)	123(2)
Wavelength (Å)	1.54178	1.54178	1.54178	0.71073	0.71073
Crystal system	Orthorhombic	Orthorhombic	Monoclinic	Monoclinic	Triclinic
Space group	$P2_12_12_1$	$P2_12_12_1$	$P2_1/c$	$P2_1/c$	P-1
a, *b*, *c* (Å)	5.9662(4) 9.2196(5) 24.3550(12)	6.0647(6) 7.6971(6) 30.801(3)	11.5002(8) 6.2421(4) 11.7468(9)	14.0221(14) 6.0437(7) 10.5529(10)	7.4314(6) 10.0392(8) 13.5335(13)
α, β, γ (°)	90 90 90	90 90 90	90.00 94.996(5) 90.00	90.00 91.539(10) 90.00	82.833(7) 82.075(8) 88.632(7)
Volume ($Å^3$)	1339.67(13)	1437.8(2)	840.04(10)	893.99(16)	992.19(15)
Z, Z'	4, 1	4, 1	2, 0.5	2, 0.5	2, 1
Density (g cm^{-3})	1.400	1.369	1.283	1.310	1.288
Crystal size (mm^3)	0.25 x 0.04 x 0.005	0.16 x 0.12 x 0.002	0.14 x 0.12 x 0.005	0.32 x 0.14 x 0.02	0.3 x 0.1 x 0.06
Reflections collected	13242	16782	8257	4138	13409
Independent reflections	2223 [R(int) = 0.0878]	2595 [R(int) = 0.1004]	1509 [R(int) = 0.0470]	1965 [R(int) = 0.0415]	4670 [R(int) = 0.0580]
Goodness-of-fit on F^2	1.139	1.049	1.133	1.168	1.057
Final R indices [I>2sigma(I)]	R1=0.0719 wR2=0.1809	R1=0.1134 wR2=0.3412	R1=0.0879 wR2=0.2610	R1=0.0647 wR2=0.1510	R1=0.0636 wR2=0.1621
R indices (all data)	R1=0.0795 wR2=0.1857	R1=0.1327 wR2=0.3637	R1=0.1222 wR2=0.2956	R1=0.0839 wR2=0.1611	R1=0.0799 wR2=0.1860

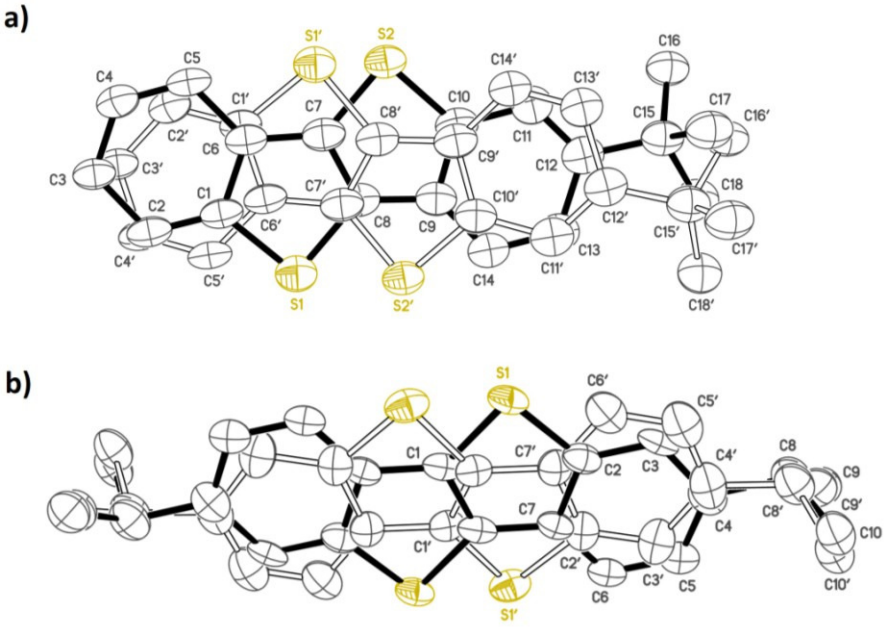

Figure S2. Visualization of the disorder present in the solid state packing of a) **tBu-BTBT** and b) **diiPr-BTBT**. The structures of **tBu-BTBT** and **diiPr-BTBT** exhibit whole molecule disorder, in which the respective molecules are flipped by *ca* 180°.

Table S4. Attachment energies and corresponding percentage of total facet area of the most dominant faces in the crystal growth morphology of the different end-capped BTBTs.

	hkl	d_{hkl} (Å)	E_{att} (kJ mol^{-1})	% total facet area
iPr-BTBT	{011}	8.6	-177.8	41.0
	{002}	12.2	-149.9	33.3
	{101}	5.8	-275.7	22.3
	{110}	5.0	-307.1	3.2
	{11-1}	4.9	-315.5	0.1
	{111}	4.9	-315.5	0.1

	hkl	d_{hkl} (Å)	E_{att} (kJ mol^{-1})	% total facet area
tBu-BTBT	{002}	15.4	-75.7	61.5
	{011}	7.5	-216.3	19.3
	{101}	6.0	-302.1	10.5
	{110}	4.8	-315.1	8.7

	hkl	d_{hkl} (Å)	E_{att} (kJ mol^{-1})	% total facet area
diiPr-BTBT	{100}	11.5	-64.0	54.2
	{011}	5.5	-169.0	19.5
	{11-1}	5.1	-161.9	11.5
	{10-2}	5.4	-179.9	9.3
	{002}	5.9	-206.7	3.7
	{110}	5.5	-175.3	1.7
	{104}	2.8	-211.3	0.1

	hkl	d_{hkl} (Å)	E_{att} (kJ mol^{-1})	% total facet area
ditBu-BTBT	{100}	14.0	-49.4	66.5
	{011}	5.2	-208.8	10.8
	{11-1}	4.9	-197.5	10.5
	{10-2}	5.0	-220.5	7.1
	{110}	5.5	-211.7	2.7
	{002}	5.3	-242.3	2.4

	hkl	d_{hkl} (Å)	E_{att} (kJ mol^{-1})	% total facet area
diTMS-BTBT	{001}	13.3	57.7	60.3
	{100}	7.4	159.0	15.3
	{010}	10.0	191.2	13.3
	{110}	5.9	198.3	5.6
	{1-11}	5.5	193.7	3.9
	{1-10}	5.9	219.2	0.8
	{01-1}	7.5	175.3	0.5
	{101}	6.9	176.6	0.3

Table S5. DFT-calculated internal reorganization energies associated to positive (λ_{i+}) and negative (λ_{i-}) polarons.

Compound	λ_+ [eV]	λ_- [eV]
iPr-BTBT	0.24	0.30
tBu-BTBT	0.24	0.30
diiPr-BTBT	0.24	0.30
ditBu-BTBT	0.25	0.34
diTMS-BTBT	0.29	0.42

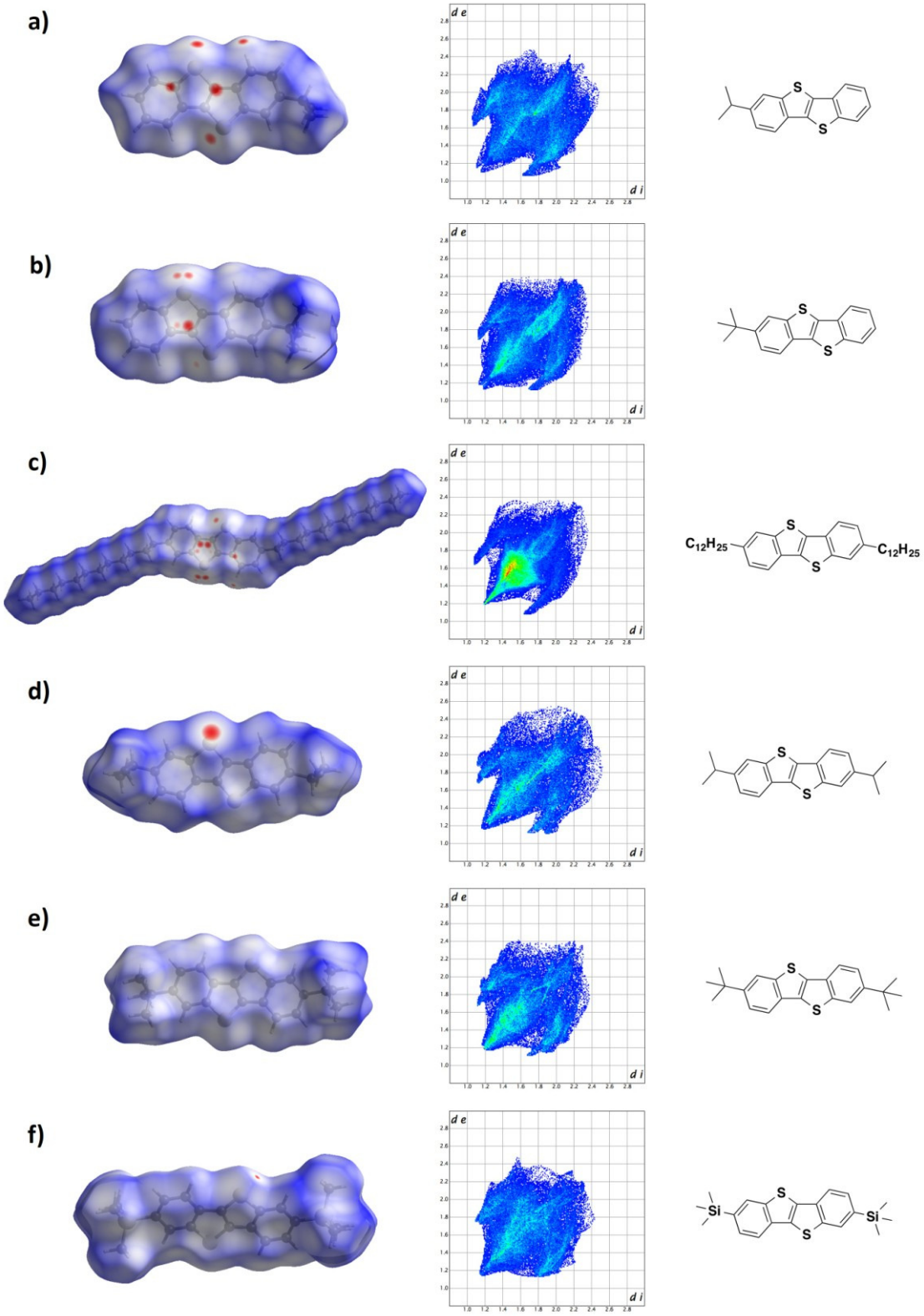

Figure S3. Hirshfeld surfaces and relative fingerprint plots for **C12-BTBT** and the different bulky end-capped BTBTs mapped over a d_{norm} range of -0.4 to 1.4 Å.

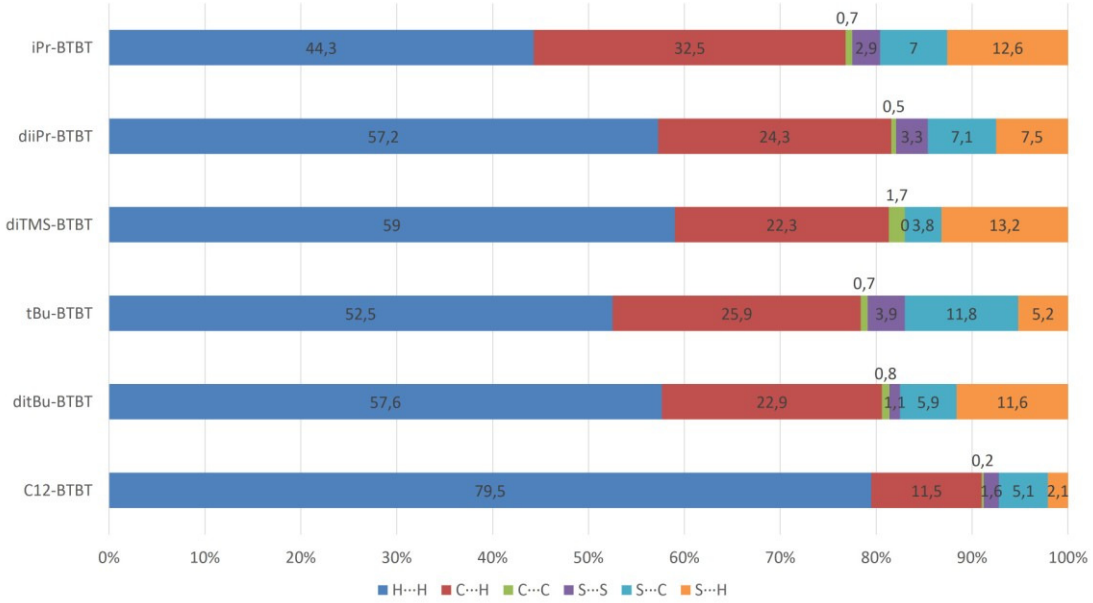

Figure S4. Percentage contributions to the Hirshfeld surface area for the various close intermolecular contacts for the different BTBT derivatives.

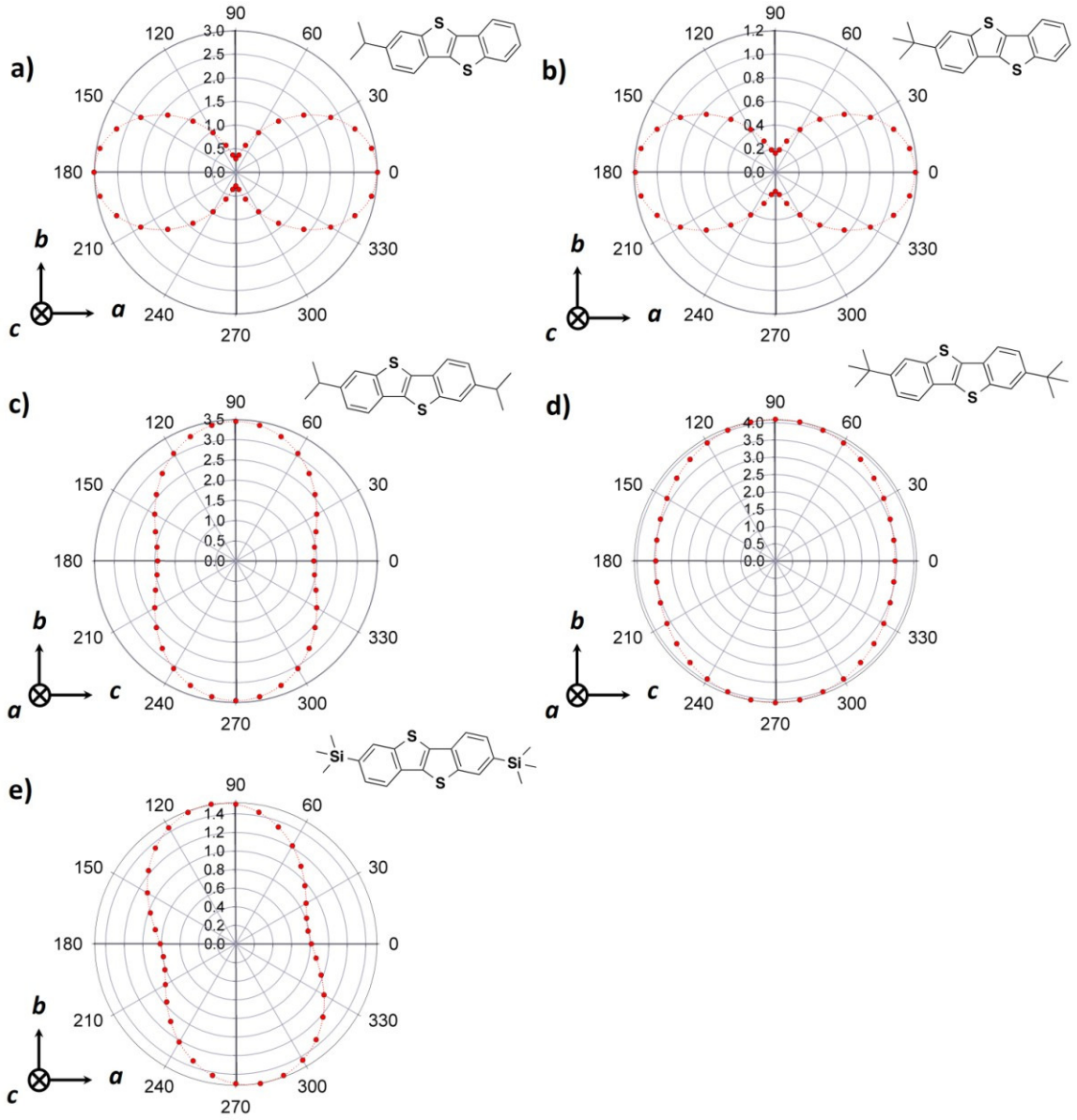

Figure S5. Calculated field-effect mobility anisotropy as a function of the crystal packing for the different bulky end-capped BTBTs.

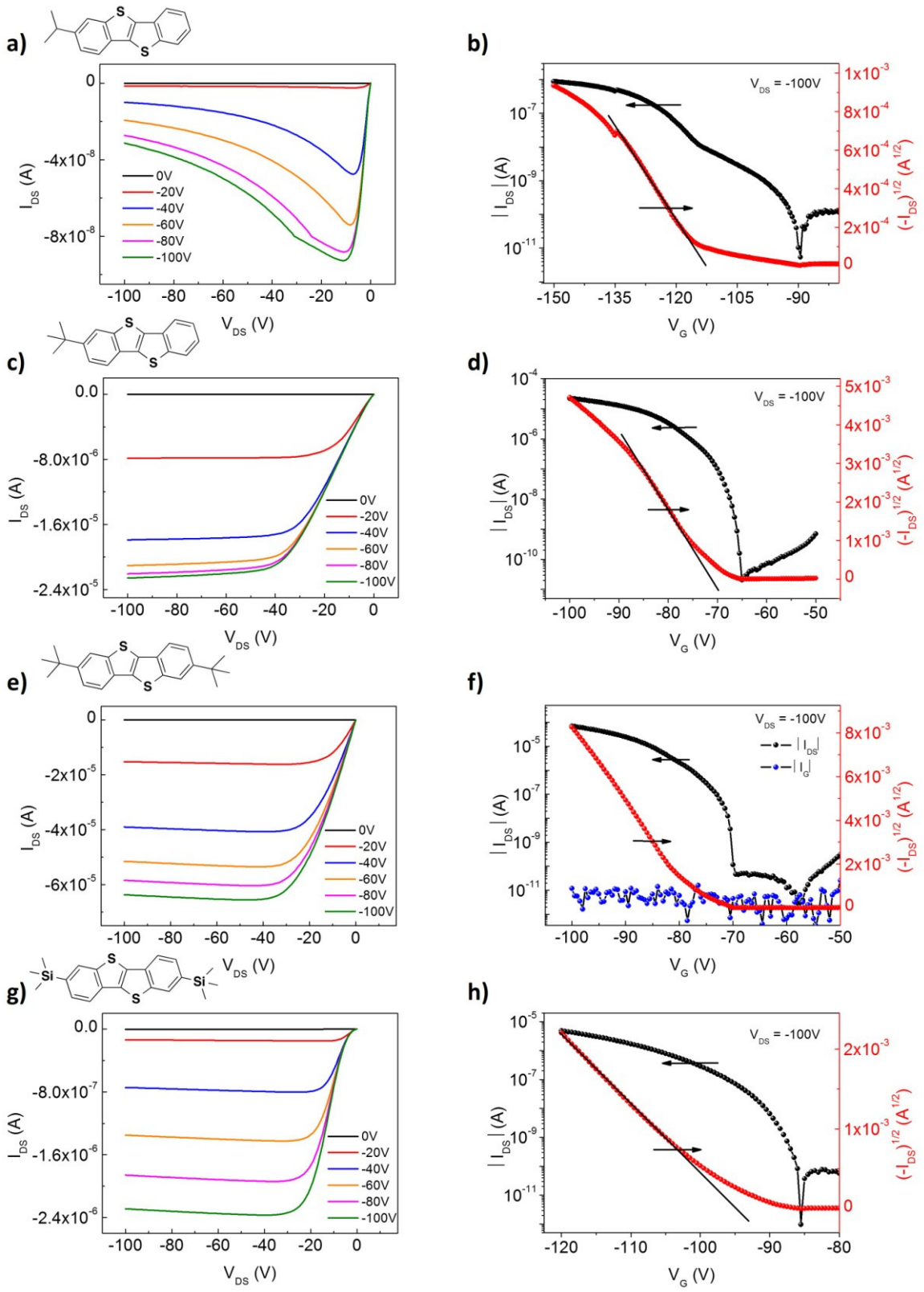

Figure S6. Output and transfer (in the saturation regime) characteristics of a device of a), b) **iPr-BTBT** presenting a channel width of 147 µm and a field-effect mobility of 0.08 $cm^2 V^{-1} s^{-1}$; c), d) **tBu-BTBT** presenting a channel width of 148 µm and a field-effect mobility of 2.1 $cm^2 V^{-1} s^{-1}$; e), f) **ditBu-BTBT** presenting a channel width of 125 µm and a field-effect mobility of 9 $cm^2 V^{-1} s^{-1}$; g), h) **diTMS-BTBT** presenting a channel width of 289 µm and a field-effect mobility of 0.2 $cm^2 V^{-1} s^{-1}$.

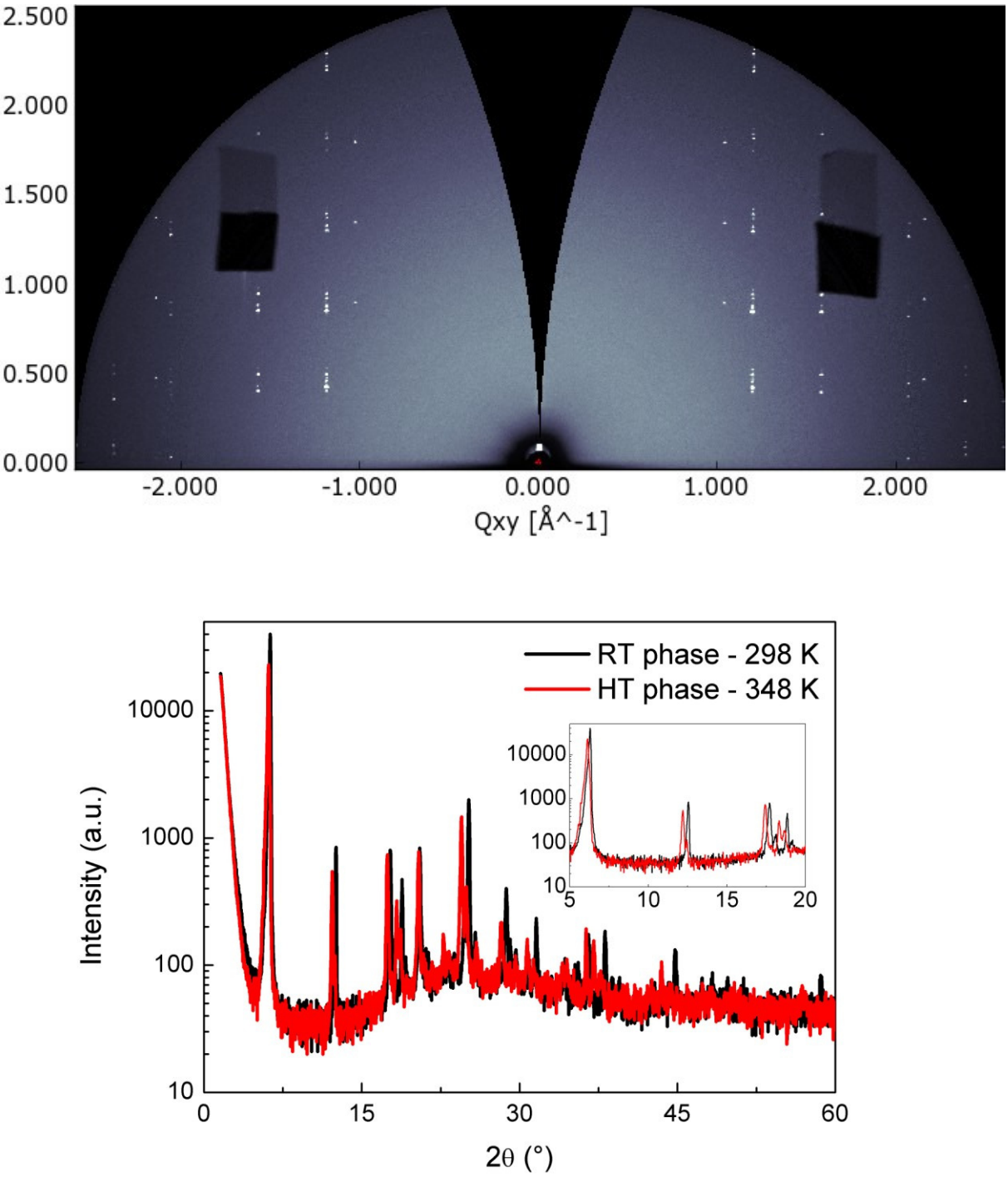

Figure S7. Room temperature GIXD diffraction pattern of a PVT grown single crystal of **ditBu-BTBT** (top). The two black holes in the GIXD pattern result from the use of metal pieces to block the diffraction from silicon in order to protect the detector. Specular X-ray diffractograms of a **ditBu-BTBT** powder sample in the room (298 K) and high temperature phase (348 K) (bottom).

Table S6. Unit cell parameters of the different crystalline phases of **ditBu-BTBT**

	Room T° phase	High T° phase	Room T° phase	High T° phase
Sample	Powder	Powder	Single crystal used for device	Thin film
Collection	Bruker D8	Bruker D8	SSRL 1-5	SSRL 11-3
Temperature (K)	298	348	298	353
Wavelength (Å)	1.5418	1.5418	0.97395	0.97395
Crystal system	Monoclinic	Monoclinic	Monoclinic	Monoclinic
Space group	$P2_1/c$	$P2_1/c$	$P2_1/c$	$P2_1/c$
a, *b*, *c* (Å)	14.1949(7) 6.2583(7) 10.7452(1)	14.6347(8) 6.3065(7) 10.4222(12)	13.965 6.104 10.569	14.538 6.246 10.387
α, β, γ (°)	90.00 91.833(12) 90.00	90.00 93.686(9) 90.00	90.03 92.668 89.78	90.12 93.658 89.78
Volume ($Å^3$)	954(1)	959(1)	899.9	941
Z, Z'	2, 0.5	2, 0.5	2, 0.5	2, 0.5
Density (g cm^{-3})	1.227	1.221	1.301	1.244

Table S7. Performances of PVT grown single crystals of **ditBu-BTBT** using only gold electrodes and 7 nm V_2O_5 doped gold contacts extracted from 4 and 16 devices respectively.

Compound	Contacts	μ_{max} [$cm^2 V^{-1} s^{-1}$]	μ [$cm^2 V^{-1} s^{-1}$]	V_{th} (V)	I_{on}/I_{off}
ditBu-BTBT	40 nm Au	0.41	0.17±0.18	-84.3±4.2	$1.5\ 10^5$
ditBu-BTBT	7 nm V_2O_5 40nm Au	10.6	5.0±3.0	-74.1±6.7	$1.0\ 10^8$

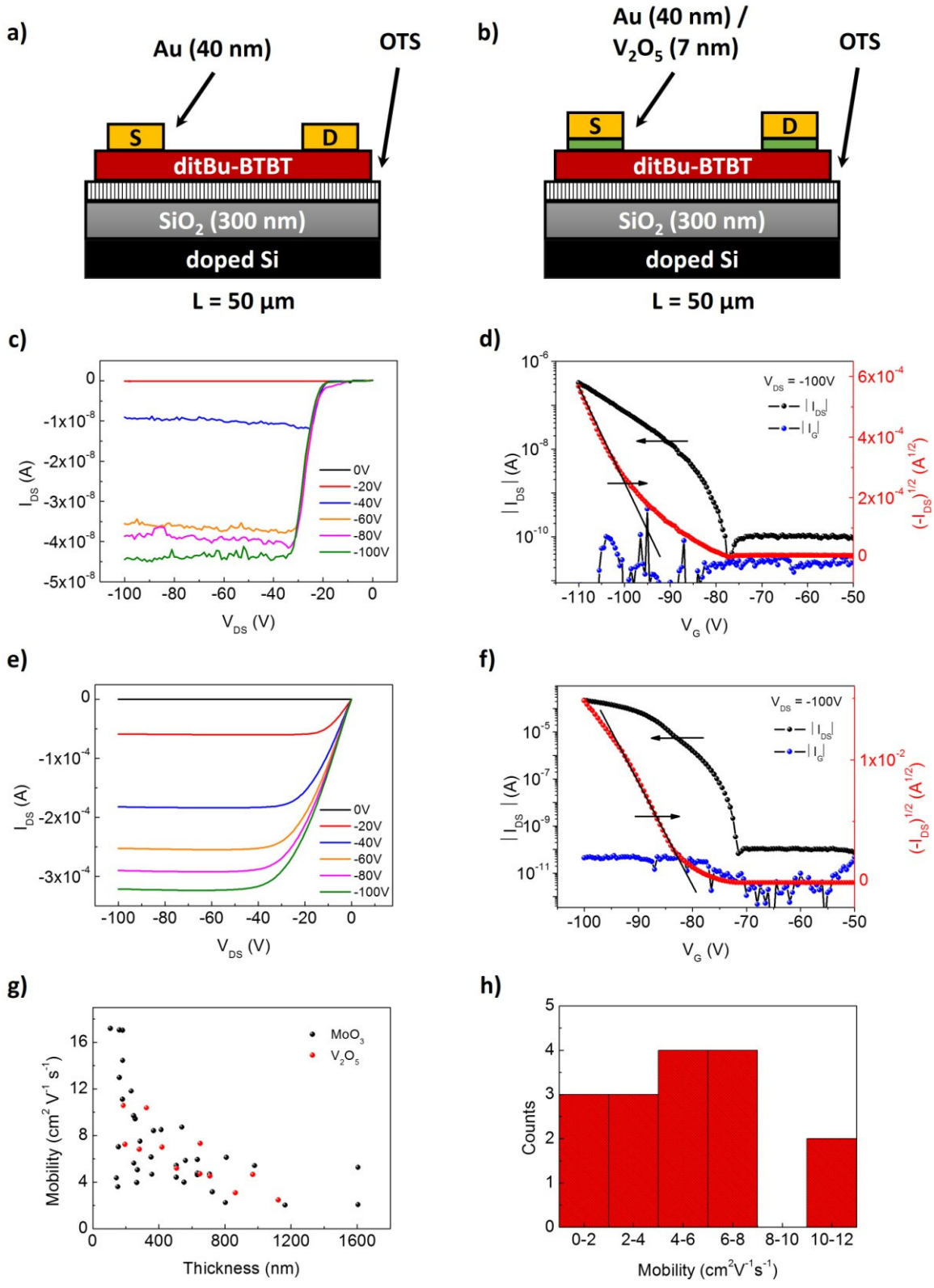

Figure S8. a), b) Schematic of a device using Au contacts and V_2O_5 and Au contacts (not to scale). c), d) output and transfer (in the saturation regime) characteristics of a **ditBu-BTBT** device with Au contacts presenting a channel width of 158 µm and a field-effect mobility of 0.2 $cm^2\ V^{-1}\ s^{-1}$. e), f) output and transfer (in the saturation regime) characteristics of a **ditBu-BTBT** device with V_2O_5 and Au contacts presenting a channel width of 545 µm and a field-effect mobility of 10.4 $cm^2\ V^{-1}\ s^{-1}$. f) Thickness dependence of the field-effect mobility. g) Mobility histogram of the 16 **ditBu-BTBT** devices using V_2O_5 and Au contacts.

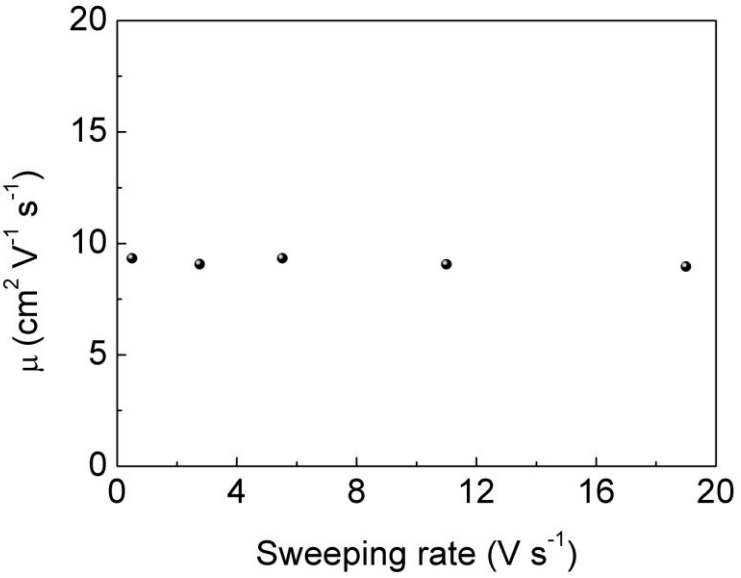

Figure S9. Gate voltage sweep rate dependence of the nominal mobility of a **ditBu-BTBT** device presenting a field-effect mobility of 9 $cm^2 V^{-1} s^{-1}$.

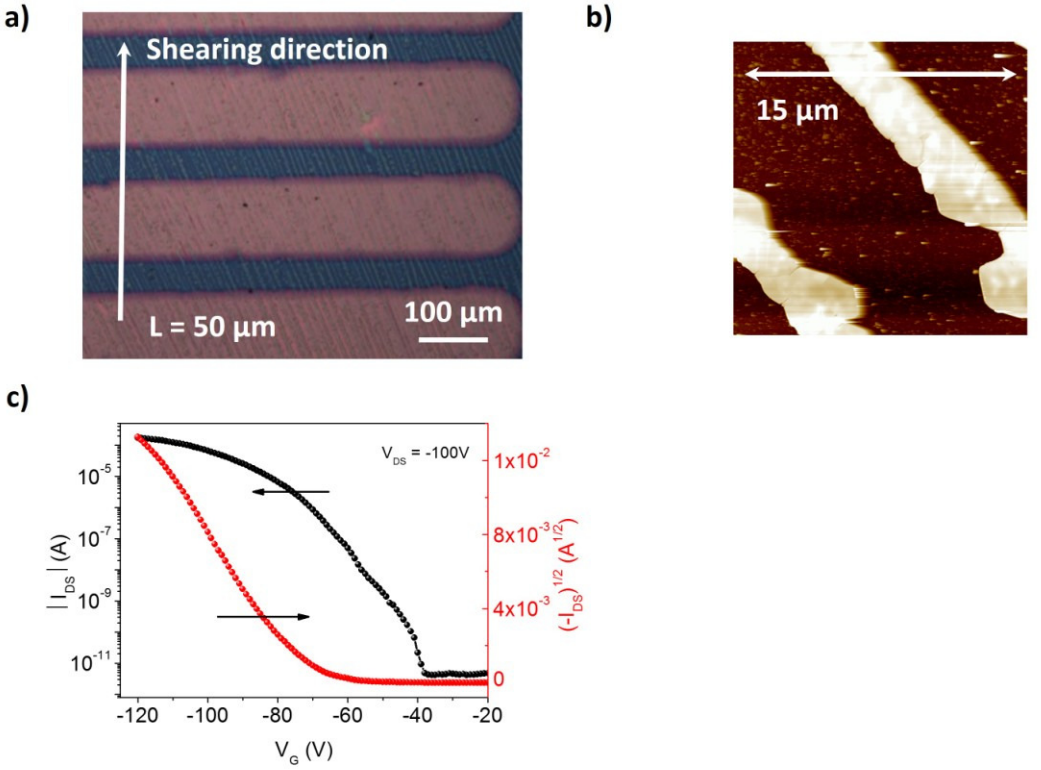

Figure S10. a), b) Optical micrograph and AFM image of a **ditBu-BTBT** film coated from its tetralin solution (2 mg ml^{-1}) at a shearing speed of 0.4 mm s^{-1}. c) Transfer (in the saturation regime) characteristic of a solution-sheared film presenting a field-effect mobility of 3.7 cm^2 V^{-1} s^{-1} (channel width of 1 mm).

[1] H. Sirringhaus, Advanced Materials 2014, 26, 1319.
[2] G. Schweicher, Y. Olivier, V. Lemaur, Y. H. Geerts, Israel Journal of Chemistry 2014, 54, 595.
[3] V. C. Sundar, J. Zaumseil, V. Podzorov, E. Menard, R. L. Willett, T. Someya, M. E. Gershenson, J. A. Rogers, Science 2004, 303, 1644.
[4] H. Minemawari, T. Yamada, H. Matsui, J. Tsutsumi, S. Haas, R. Chiba, R. Kumai, T. Hasegawa, Nature 2011, 475, 364.
[5] a) A. Briseno, S. Mannsfeld, M. Ling, S. Liu, R. Tseng, C. Reese, M. Roberts, Y. Yang, F. Wudl, Z. Bao, Nature 2006, 444, 913; b) O. Goto, S. Tomiya, Y. Murakami, A. Shinozaki, A. Toda, J. Kasahara, D. Hobara, Advanced Materials 2012, 24, 1117; c) S. Liu, W. Wang, A. Briseno, S. Mannsfeld, Z. Bao, Advanced Materials 2009, 21, 1217; d) K. Nakayama, Y. Hirose, J. Soeda, M. Yoshizumi, T. Uemura, M. Uno, W. Li, M. J. Kang, M. Yamagishi, Y. Okada, Advanced Materials 2011, 23, 1626; e) L. Jiang, H. Dong, W. Hu, Journal of Materials Chemistry 2010, 20, 4994.
[6] M. M. Payne, S. R. Parkin, J. E. Anthony, C.-C. Kuo, T. N. Jackson, Journal of the American Chemical Society 2005, 127, 4986.
[7] J. Chen, C. K. Tee, M. Shtein, D. C. Martin, J. Anthony, Organic Electronics 2009, 10, 696.
[8] H. Ebata, T. Izawa, E. Miyazaki, K. Takimiya, M. Ikeda, H. Kuwabara, T. Yui, Journal of the American Chemical Society 2007, 129, 15732.
[9] T. Yamamoto, K. Takimiya, Journal of the American Chemical Society 2007, 129, 2224.
[10] W. Xie, K. Willa, Y. Wu, R. Häusermann, K. Takimiya, B. Batlogg, C. D. Frisbie, Advanced Materials 2013, 25, 3478; Y. Yuan, G. Giri, A. L. Ayzner, A. P. Zoombelt, S. C. Mannsfeld, J. Chen, D. Nordlund, M. F. Toney, J. Huang, Z. Bao, Nature communications 2014, 5.
[11] a) M. J. Kang, I. Doi, H. Mori, E. Miyazaki, K. Takimiya, M. Ikeda, H. Kuwabara, Advanced Materials 2011, 23, 1222; b) K. Takimiya, S. Shinamura, I. Osaka, E. Miyazaki, Advanced Materials 2011, 23, 4347; c) K. Takimiya, I. Osaka, T. Mori, M. Nakano, Accounts of chemical research 2014; d) C. Ruzie, J. Karpinska, A. R. Kennedy, Y. H. Geerts, The Journal of organic chemistry 2013, 78, 7741; e) C. Niebel, Y. Kim, C. Ruzié, J. Karpinska, B. Chattopadhyay, G. Schweicher, A. Richard, V. Lemaur, Y. Olivier, J. Cornil, A. R. Kennedy, Y. Diao, W.-Y. Lee, S. Mannsfeld, Z. Bao, Y. H. Geerts, Journal of Materials Chemistry C 2015, 3, 674.
[12] a) T. Okamoto, C. Mitsui, M. Yamagishi, K. Nakahara, J. Soeda, Y. Hirose, K. Miwa, H. Sato, A. Yamano, T. Matsushita, Advanced Materials 2013, 25, 6392; b) C. Mitsui, T. Okamoto, M. Yamagishi, J. Tsurumi, K. Yoshimoto, K. Nakahara, J. Soeda, Y. Hirose, H. Sato, A. Yamano, Advanced Materials 2014, 26, 4546.
[13] C. Reese, M. E. Roberts, S. R. Parkin, Z. Bao, Advanced Materials 2009, 21, 3678.
[14] C. Reese, M. E. Roberts, S. R. Parkin, Z. Bao, Applied Physics Letters 2009, 94, 202101.
[15] A. Kreyes, A. Mourran, Z. Hong, J. Wang, M. Möller, F. Gholamrezaie, W. C. Roelofs, D. M. de Leeuw, U. Ziener, Chemistry of Materials 2013, 25, 2128.
[16] P. Hartman, P. Bennema, Journal of Crystal Growth 1980, 49, 145.
[17] A. Troisi, G. Orlandi, Physical review letters 2006, 96, 086601; M. Hultell, S. Stafström, Chemical physics letters 2006, 428, 446.
[18] M. C. Gwinner, R. D. Pietro, Y. Vaynzof, K. J. Greenberg, P. K. Ho, R. H. Friend, H. Sirringhaus, Advanced Functional Materials 2011, 21, 1432.
[19] C. Mitsui, J. Soeda, K. Miwa, H. Tsuji, J. Takeya, E. Nakamura, Journal of the American Chemical Society 2012, 134, 5448.

[20] H. Jiang, K. J. Tan, K. K. Zhang, X. Chen, C. Kloc, Journal of Materials Chemistry 2011, 21, 4771.
[21] Y. Chen, B. Lee, H. Yi, S. Lee, M. Payne, S. Pola, C.-H. Kuo, Y.-L. Loo, J. Anthony, Y. Tao, Physical Chemistry Chemical Physics 2012, 14, 14142.
[22] H. Jiang, C. Kloc, MRS bulletin 2013, 38, 28.
[23] C. Reese, W.-J. Chung, M.-m. Ling, M. Roberts, Z. Bao, Applied physics letters 2006, 89, 202108.
[24] Oxford Diffraction "CrysAlisPro", Oxford Diffraction, Yarnton, UK 2010.
[25] a) S. Parkin, B. Moezzi, H. Hope, Journal of applied crystallography 1995, 28, 53; b) Bruker "APEX2", Bruker-AXS Inc., Madiwon, WI, USA 2012.
[26] G. M. Sheldrick, Acta Crystallographica Section A: Foundations of Crystallography 2008, 64, 112.
[27] F. Hirshfeld, Theoretica chimica acta 1977, 44, 129.
[28] M. A. Spackman, J. J. McKinnon, CrystEngComm 2002, 4, 378.
[29] S. Wolff, D. Grimwood, J. McKinnon, M. Turner, D. Jayatilaka, M. Spackman, University of Western Australia 2012.
[30] Materials-Studio-Modeling, Accelrys Software Inc, San Diego, CA 2009.
[31] H. Sun, The Journal of Physical Chemistry B 1998, 102, 7338.
[32] Y. Ito, A. A. Virkar, S. Mannsfeld, J. H. Oh, M. Toney, J. Locklin, Z. Bao, Journal of the American Chemical Society 2009, 131, 9396.
[33] L. Patrone, V. Gadenne, S. Desbief, Langmuir 2010, 26, 17111.
[34] H. Li, B. C. K. Tee, J. J. Cha, Y. Cui, J. W. Chung, S. Y. Lee, Z. Bao, Journal of the American Chemical Society 2012, 134, 2760.
[35] S. C. B. Mannsfeld, M. L. Tang, Z. Bao, Advanced Materials 2011, 23, 127.
[36] V. Coropceanu, J. Cornil, D. da Silva Filho, Y. Olivier, R. Silbey, J. Bredas, Chemical Reviews 2007, 107, 926.
[37] V. Lemaur, D. da Silva Filho, V. Coropceanu, M. Lehmann, Y. Geerts, J. Piris, M. Debije, A. van de Craats, K. Senthilkumar, L. Siebbeles, Journal of the American Chemical Society 2004, 126, 3271.
[38] N. G. Martinelli, J. Idé, R. S. Sánchez-Carrera, V. Coropceanu, J.-L. Brédas, L. Ducasse, F. Castet, J. Cornil, D. Beljonne, The Journal of Physical Chemistry C 2010, 114, 20678.
[39] G. Te Velde, F. M. Bickelhaupt, E. J. Baerends, C. Fonseca Guerra, S. J. van Gisbergen, J. G. Snijders, T. Ziegler, Journal of Computational Chemistry 2001, 22, 931.
[40] E. F. Valeev, V. Coropceanu, D. A. da Silva Filho, S. Salman, J.-L. Brédas, Journal of the American Chemical Society 2006, 128, 9882; L. Viani, Y. Olivier, S. Athanasopoulos, D. A. da Silva Filho, J. Hulliger, J. L. Brédas, J. Gierschner, J. Cornil, ChemPhysChem 2010, 11, 1062.